Research Square

Preprints are preliminary reports that have not undergone peer review.
They should not be considered conclusive, used to inform clinical practice,
or referenced by the media as validated information.

Kandil Concrete-Faced Rockfill Dam and its Response to the 2023 Kahramanmaraş Earthquake Sequence from Strong-Motion Records, Instrumentation, and Underwater Inspection

Murat Eröz

murat.eroz@enerjisauretim.com

Enerjisa Enerji Üretim A.Ş. https://orcid.org/0000-0002-6328-7323

Research Article

Keywords: Concrete-faced rockfill dam, seismic performance, response spectra, dam instrumentation, remotely operated vehicle (ROV) inspection, 2023 Kahramanmaraş earthquakes

Posted Date: November 11th, 2026

DOI: https://doi.org/10.21203/rs.3.rs-11468001/v1

License: This work is licensed under a Creative Commons Attribution 4.0 International License.
Read Full License

Kandil Concrete-Faced Rockfill Dam and its Response to the 2023 Kahramanmaraş Earthquake Sequence from Strong-Motion Records, Instrumentation, and Underwater Inspection

Murat Eröz[1,*]

[1]Enerjisa Üretim A.Ş., Asset Management and Sustainability Directorate, Istanbul, Türkiye

*Corresponding author. Email: murat.eroz@enerjisauretim.com. ORCID iD 0000-0002-6328-7323

Acknowledgments

The author thanks Enerjisa Üretim A.Ş. for access to the dam safety records of Kandil Dam and its dam safety and instrumentation teams for collecting the field data and carrying out the remotely operated vehicle survey. The author gratefully acknowledges Kemal Tuncer, Senior Dam Safety Expert at Enerjisa Üretim A.Ş., for his review of the dam behavior assessment and his advice on the engineering interpretation of the monitoring records, and Murat Işıldak, Expert Structural Design Engineer at Enerjisa Üretim A.Ş., for the verification of the instrumentation data and of all numerical values against the source records. The author acknowledges Editage (www.editage.com) for English language editing.

Abstract

This study evaluates the response of the 103-m-high Kandil concrete-faced rockfill dam (CFRD) to the Mw 7.7 Pazarcık and Mw 7.6 Elbistan earthquakes on February 6, 2023, the second of which was 7.3 km away, against the design predictions and known damage mechanisms for CFRDs. Kandil Dam is the only high CFRD for which abutment and crest strong-motion records exist in

the near field of the sequence. Data were collected via 190 monitoring instruments, a remotely operated vehicle survey of the face slab joints, and the reconstructed design basis and accelerogram. The abutment motion exceeded the maximum credible earthquake acceleration of the design by a factor of 1.6; however, the scaled design accelerogram was only exceeded for periods of less than 0.3 s. At the fundamental period of the dam, the demand was approximately half the design input, and the crest acceleration remained below the prediction. The fundamental period increased by approximately 30% under strong shaking, consistent with strain-dependent softening of the rockfill without large-scale instability. Permanent downstream movements of the upper shell reached 0.4 m and decayed with depth. Crest settlement was 0.06% and 0.12% of the height at the parapet and crest edge, respectively; residual joint movements were a few millimeters; seepage showed no sustained increase; and the transient increase in foundation pore pressure decayed over days. The slab crushing and seepage increase observed at other CFRDs did not develop. The results provide a benchmark for CFRD verification and support instrumentation, inspection, and reporting requirements near active faults.

Keywords: Concrete-faced rockfill dam, seismic performance, response spectra, dam instrumentation, remotely operated vehicle (ROV) inspection, 2023 Kahramanmaraş earthquakes

1. Introduction

During earthquakes, embankment dams typically fail owing to slope instability, liquefaction, and overtopping after crest deformation (Seed and Lee 1973; Singh et al. 2005; Chen et al. 2012; Yamaguchi et al. 2012). A concrete-faced rockfill dam (CFRD) places the water barrier, consisting of reinforced concrete face slabs, on the upstream face of a free-draining rockfill embankment; therefore, in well-compacted rockfill, such as that at Kandil Dam, undrained loading, liquefaction,

and strength loss are not expected. The seismic damage mechanisms documented for CFRDs include cracking of the slabs, opening of their joints, and an increase in leakage (Sherard and Cooke 1987). When the 156-m-high Zipingpu CFRD was shaken beyond its design seismicity by the 2008 Wenchuan earthquake, it sustained crushing of the face slabs along the vertical joints, damage to the perimeter joint waterstops, increased seepage, and more than 70 cm of crest settlement; however, it remained structurally safe (Zhang et al. 2015). By contrast, the Ishibuchi CFRD showed only minor damage in the 2008 Iwate–Miyagi Nairiku and 2011 Tohoku earthquakes (USSD 2014; Yamaguchi et al. 2012). These cases underpin the procedures for estimating the earthquake-induced permanent deformation of CFRDs (Swaisgood 2014; Durmaz and Ülgen 2021); however, few dams have experienced shaking above their design basis (USSD 2014), and records of high CFRDs under near-fault motion above their design inputs are scarce.

The 2023 Kahramanmaraş earthquake sequence, which consisted of two Mw 7.7 and Mw 7.6 events within 9 h, caused extensive damage across eleven provinces (Avcil et al. 2024) and shook an unusually large dam inventory. Cetin et al. (2024) documented the performance of the 140 dams in the influence zone, 60 of which were within 50 km of the ruptures, and reported that all retained their reservoirs, that 28 earthfill and rockfill dams developed permanent deformations with crack widths of more than 5 cm, and that the deformations increased toward the rupture. Bayraktar et al. (2024a) described the 17 damaged dams, including a single CFRD with minor crest cracks, and estimated that the crest accelerations were approximately four times the free-field values because no records existed at those sites. Moreover, Bayraktar et al. (2024b) analyzed the records of three instrumented undamaged dams, including the 88-m-high Kavşak Bendi CFRD, which was more than 130 km from both epicenters. Ozkula et al. (2023) documented crest cracking and lateral displacements of 0.15 m to several meters at three earth dams and called for systematic monitoring

to identify the mechanisms in the dams that were damaged and in those that performed well. Hariri-Ardebili and Tosun (2024) identified the lack of near-field records as the main obstacle to a quantitative evaluation. None of these studies present a continuous multi-parameter record of a high CFRD in the near field of the Elbistan rupture combined with an underwater inspection of the face slab joints.

Kandil Dam, a 103-m-high CFRD located 7.3 km from the Elbistan epicenter and approximately 3 km from the Çardak Fault that generated it, fills this gap. Its peak accelerations were reported by Cetin et al. (2024); however, the records, 190 operational instruments, and inspection of the submerged face slab joints by a remotely operated vehicle (ROV) four weeks after the events have not been analyzed. The objective of this study is to evaluate the recorded performance of a high CFRD under near-fault shaking above its design basis against the documented design predictions and the known damage mechanisms for CFRDs, and to explain the differences from the records. The reference for the evaluation is reconstructed retrospectively from the design documents (Section 2.3); for the maximum credible earthquake (MCE) level, this predicts a crest acceleration of 1.9 g, permanent crest displacements of approximately 21 cm downstream and 24 cm vertically, joint movements of up to 16 mm, and slab stresses of up to 15 MPa. These predictions, combined with the documented mechanisms for CFRDs under strong shaking, indicate possible outcomes of motion above the design level, rather than predictions. The specific objectives are to (1) reconstruct the design basis; (2) characterize the recorded motions by response spectra, transfer functions, strain-compatible stiffness, and sliding block checks; (3) document the measured response and post-earthquake condition of the dam and submerged joints; and (4) compare the measured and predicted responses parameter by parameter, distinguishing peak dynamic predictions, permanent predictions, and residual measurements.

2. Dam, Site, and Seismic Design Basis

2.1.Embankment and face slab system

Kandil Dam is located in Ekinözü District, Kahramanmaraş Province, in the upper Ceyhan Basin. Impounding began in January 2013 and operation began in October 2013. The dam is 103 m high with a crest elevation of 1101.0 m including the parapet wall, a maximum operating level of 1097.0 m, a flood level of 1098.55 m, and a minimum operating level of 1064.0 m. The cross section and the main characteristics are given in **Fig. 1** and **Table 1.**

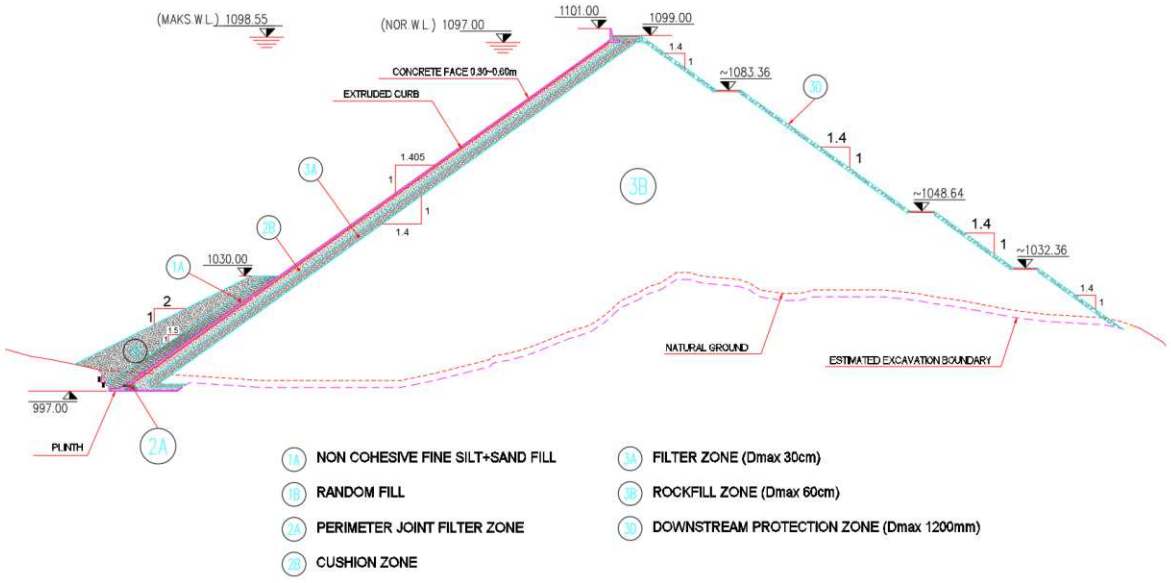


Fig. 1 Cross section of Kandil CFRD

The fill comprises the 2A peripheral joint filter, a processed sand–gravel mixture approximately 2 m behind the perimeter joint that retains fines carried by flow through an impaired waterstop, the semi-pervious 2B cushion that supports the face and limits leakage through cracks, and the 3A transition and 3B rockfill zones of serpentinite and peridotite placed in 40-cm and 60-cm layers

(Fig. 1). This fill was compacted with a 10-ton vibratory roller in at least six passes under the gradation limits and quality control tests given in **Tables S1–S4** in Online Resource 1.

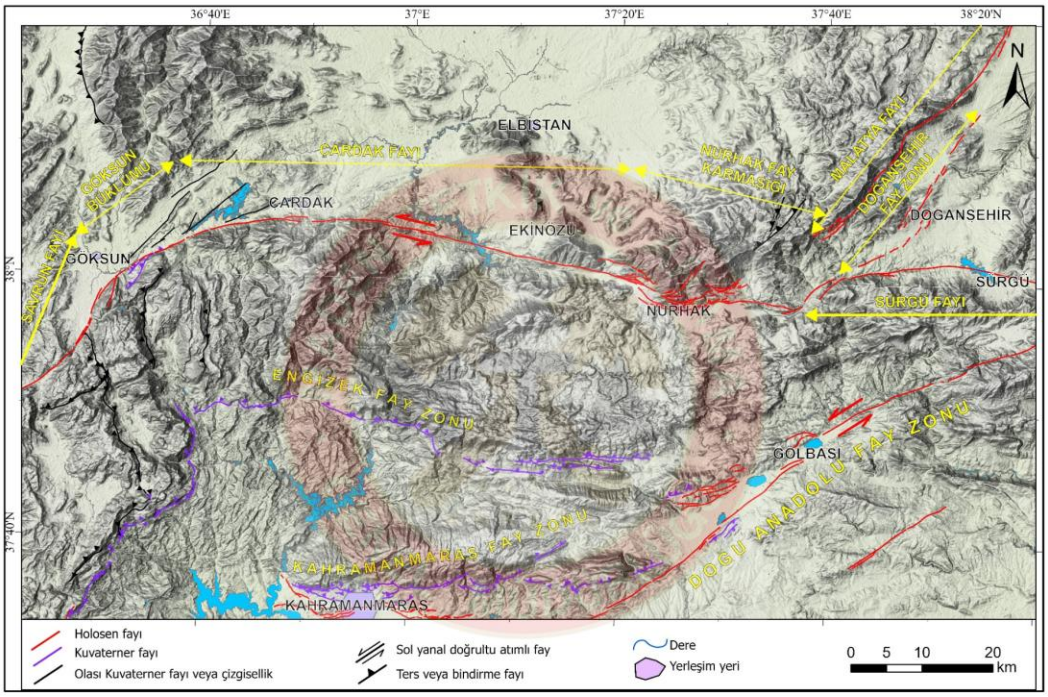
The upstream face consists of 23 slabs with a width of 15 m. The slabs are separated by 4-cm-wide compressible vertical joints, which are filled with a material with a modulus of approximately 10 MPa. The slabs are 0.30 m thick at the crest and 0.60 m at the plinth, consist of C30 concrete with a characteristic strength of 30 MPa and a modulus of 32,000 MPa, and were designed according to Turkish standards TS 500 (TSE 2000) and TS 498 (TSE 1997) and the earthquake code DBYBHY 2007 (Ministry of Public Works and Settlement 2007). Each joint carries a W-shaped copper waterstop bedded on a neoprene band, the water barrier of the joint, which is covered by a polyvinyl chloride (PVC) band filled with fly ash that acts as an expendable upper barrier (Section 6.6). The fill crest lies at El. 1099.0 m with a width of 8.7 m. The 4-m-high upstream parapet wall, which carries the face slab above the normal maximum level of 1097.0 m to El. 1101.0 m, is 12.0 m wide at the foundation level (Hidro Dizayn 2009).

2.2. Foundation geology and seismotectonic setting

Five boreholes along the plinth axis traversed serpentinized metagabbro and metadiabase. The core recovery was typically between 70% and 100%, no alluvium was found along the axis, and the plinth rests entirely on bedrock (**Fig. S1** in Online Resource 1).

The 1544 earthquake destroyed the Zitun settlement, now Göksun, and partly destroyed Elbistan (Ambraseys 1989). The nearest active structure, approximately 3 km from the dam, is the Çardak Fault, an east–west trending fault more than 85 km in length that Duman and Emre (2013) identified as the longest segment of the Sürgü–Misis Fault System (**Fig. 2**). The fault has displaced the Ceyhan River by 11 km in a left-lateral sense, and has a slip rate of 2.5 mm/year. Balkaya et

129 al. (2021a) confirmed its activity from morphometric indices, and paleoseismological trenching
130 identified two Holocene surface-rupturing earthquakes on it, the younger between 3215 ± 125 BCE
131 and 825 ± 55 CE (Balkaya et al. 2021b).



132

133 **Fig. 2** Fault map of the Kandil Dam region (Duman and Emre 2013)

134

135 ***2.3.Seismic design basis and performance objectives***

136 The seismic design basis (**Table 2**) was reconstructed from three documents, and the attribution
137 matters. The site-specific hazard study (Kaptan 2007) placed the site in the second-degree zone of
138 the Turkish seismic zonation map, 50 km from the East Anatolian Fault Zone. From a probabilistic
139 analysis, they specified an operating basis earthquake (OBE) peak ground acceleration (PGA) of
140 0.10 g with a return period of 144 years, and a maximum design earthquake (MDE) PGA of 0.18
141 g with a return period of 475 years. Therefore, the MCE was defined as an M 7.5 event based on
142 regional sources without assigning it a PGA. This analysis acknowledged the fault 2 km north of
143 the dam and accounted for it by increasing the pseudo-static coefficient from 0.11 to 0.12. The

144 Holocene surface ruptures of the Çardak Fault were documented after the design (Duman and
145 Emre 2013; Balkaya et al. 2021b). This study retains the terminology of the design documents.
146 For the retrospective assessment, it adopts the performance expectations that ICOLD Bulletin 148
147 (ICOLD 2016) attaches to the OBE—at most minor damage with continued operation—and the
148 safety evaluation earthquake (SEE)—no uncontrolled release of the reservoir with repairable
149 damage—and applies the latter to the MDE and MCE levels of the design. This mapping is the
150 interpretation of this study, not an equivalence stated by the design reports or by the Bulletin.

151 The final design (Hidro Dizayn 2009) adopted the OBE and MDE values and verified the
152 embankment slopes by pseudo-static limit equilibrium analysis against the required safety factors:
153 1.5 under static conditions, 1.2 under the OBE, and 1.0 under the MCE (**Table S5** in Online
154 Resource 1). Values of 1.549, 1.233, 1.105, and 1.067 were obtained at seismic coefficients of 0,
155 0.12, 0.18, and 0.20 with a full reservoir. A yield acceleration of 0.21 g was used for the critical
156 surface in the settlement estimates, whereas extrapolation of the tabulated factors to unity gave
157 approximately 0.235. The dynamic verification (Hidro Dizayn 2012) adopted the 1998 Adana–
158 Ceyhan record, which was scaled to 0.10, 0.18, and 0.45 g, high-frequency filtered, and applied at
159 the base of a massless rock foundation in a three-dimensional elastic perfectly plastic model with
160 the properties listed in Table 2, after the construction and reservoir loading stages. The MCE PGA
161 of 0.45 g corresponds to 1.5 times the 0.30 g effective ground acceleration of the second-degree
162 zone, which documents how the value was selected, although it is not a site-specific deterministic
163 hazard calculation. Deterministic analyses of Turkish dam sites near local source zones give
164 similar values of 0.42–0.45 g (Seyrek and Tosun 2011). The predicted MCE response (**Table 3**)
165 comprises a peak crest acceleration of 1.90 g, permanent crest displacements of 21.2 cm

downstream and 23.9 cm vertically, peak joint closures and openings of 12.3 and 15.6 mm, and a peak slab compressive stress of 14.5 MPa against 30 MPa.

3. February 6, 2023, Earthquake Sequence

According to the catalogue of the Disaster and Emergency Management Authority (AFAD 2023), the Mw 7.7 Pazarcık earthquake occurred at 04:17 local time with its epicenter 87.6 km from Kandil Dam, and the Mw 7.6 Elbistan earthquake occurred at 13:24 with its epicenter 7.3 km from Kandil Dam (**Fig. 3**). The two events caused 50,783 fatalities. The Pazarcık earthquake ruptured more than 300 km of the East Anatolian Fault with displacements of more than 6.5 m and a maximum recorded acceleration of 2178.71 gal at Pazarcık Station. The Elbistan earthquake ruptured 130 km of the Çardak Fault, the structure closest to the dam, with a maximum recorded free-field acceleration of 635.44 gal at Göksun Station. Near the ruptures, the PGA exceeded 2 g, the peak ground velocity (PGV) reached 180 cm/s, and the recorded spectra exceeded the design spectra of the Turkish codes at 0.2 and 1.0 s (Akinci et al. 2025). AFAD assigned intensities XI and X to Ekinözü district, where the dam is located. The ground motion parameters of the strongest free-field stations are listed in **Tables S6 and S7** in Online Resource 1.

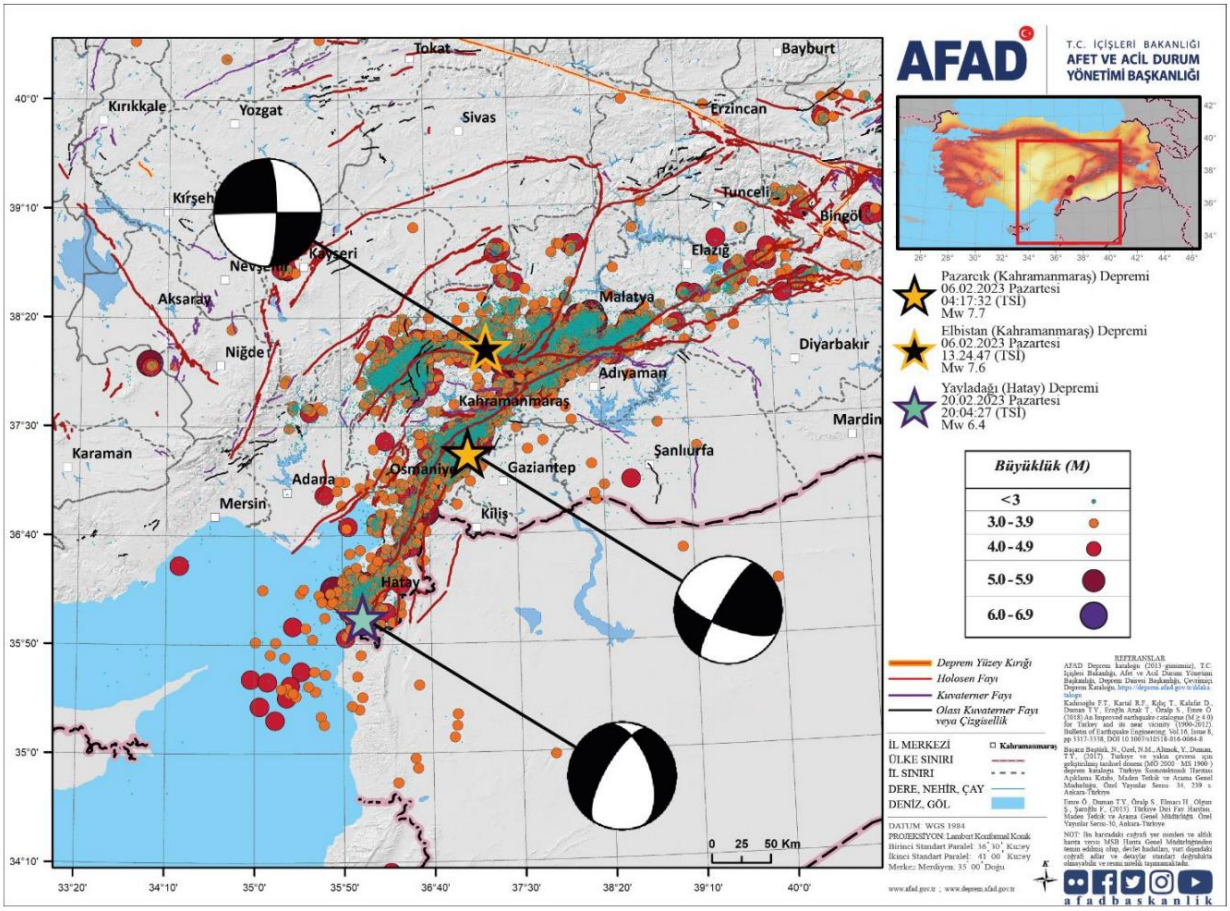


Fig. 3 February 6, 2023, Pazarcık (Kahramanmaraş) Mw: 7.7, Elbistan (Kahramanmaraş) Mw: 7.6, and Yayladağı (Hatay) Mw: 6.4 earthquakes and aftershock activity (February 6–May 6) (AFAD 2023)

4. Instrumentation and Post-Earthquake Monitoring

At Kandil Dam, 227 instrument components were installed at cross sections 0+175, 0+200, and 0+225 m, which are located at the maximum height of the dam, of which 190 were operational during the assessment (**Fig. 4**, **Figs. S2–S5** in Online Resource 1, and **Table S8** in Online Resource 1). All 29 embedded settlement cells (SCs), six with drifted baselines, and all 29 total pressure cells (TPCs) returned readings; 11 of the 12 vibrating wire piezometers (VWPs) captured the pore pressure response; the crest and foundation accelerometers, automated reservoir level gauge, V-notch weir, and complete topographic network were available; 19 of the 30 strain gauge

components were operational, with 17 of them classed as fully operational; and five of the 12 hydraulic joint meters (HJMs) returned readings. Therefore, the face slab stress and joint measurements only covered the instrumented locations. The weir and the topographic points were read manually, and the remaining instruments were read remotely. Rockfalls and road embankment failures blocked the access roads; therefore, the first inspection used remote cameras and the remotely read instruments. This was followed by an on-site visit within 6 h of the first earthquake, before the second earthquake, after which the assessment again relied on the remotely read instruments. The automated logger read the instruments once a day until 02:00 on February 6 and every 20 min from 17:10 on that day, 3 h 46 min after the Elbistan earthquake. Therefore, all instruments except the accelerometers documented residual changes that combined the two events, not the maximum response during the shaking.

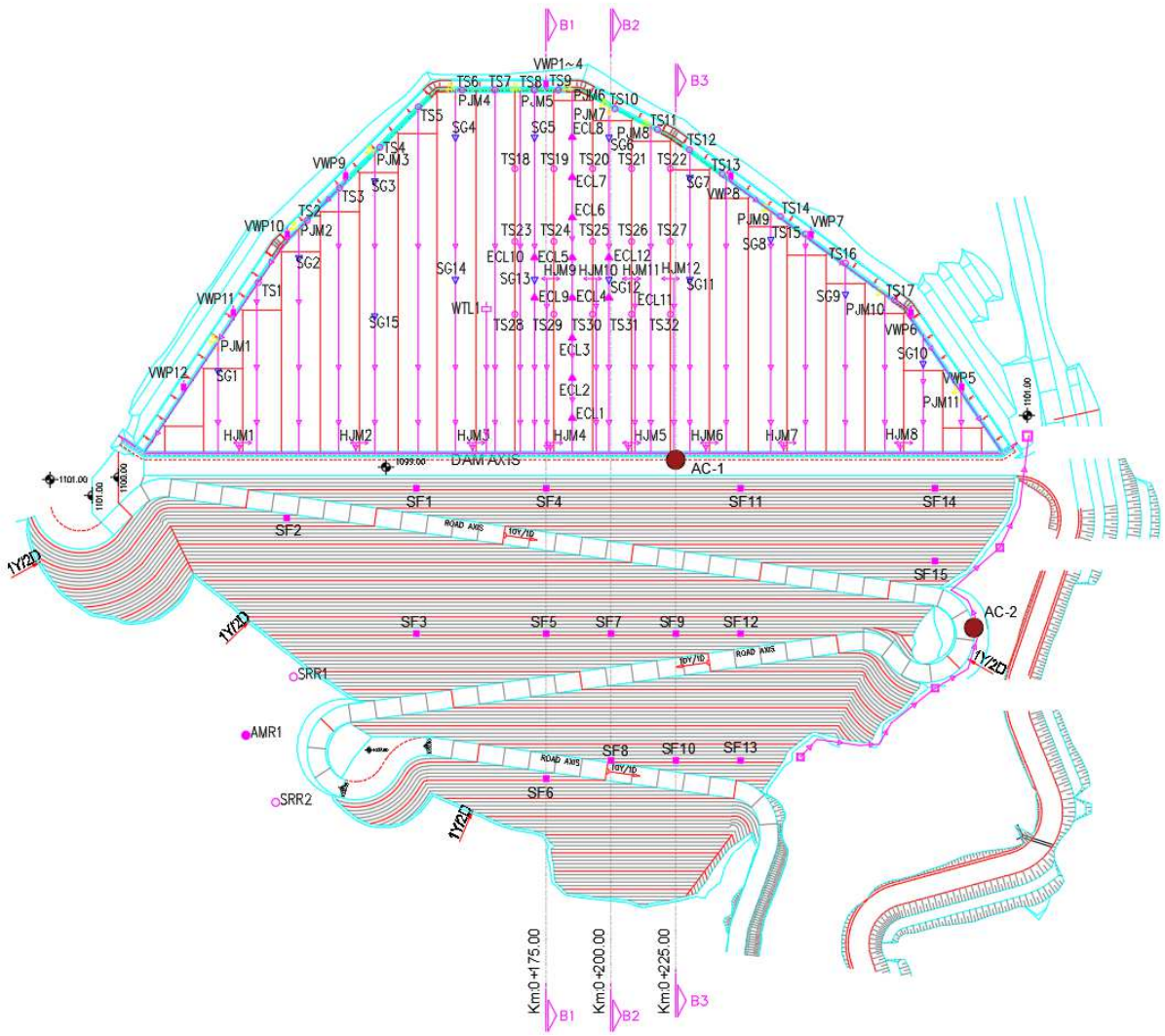


Fig. 4 Locations of the instruments

5. Recorded Motions and Dynamic Response Analysis

5.1.Records, processing, and peak values

Three-component accelerometers on rock at the right abutment and crest recorded both earthquakes at 100 samples per second with the reservoir at 1084.5 m (**Fig. 5**). The records were baseline corrected and band-pass filtered between 0.1 and 25 Hz with a fourth-order zero-phase Butterworth filter, and the horizontal components were rotated into the upstream–downstream

(primary) and dam-axis (secondary) directions; the rotation used 29° east of north, as in the design (the parapet survey gave 31°, which changed the peaks by 2.5% or less). **Table 4** lists the peak accelerations of the baseline-corrected records. During the Elbistan earthquake, the abutment rock reached peak accelerations of 0.718, 0.845, and 0.551 g in the primary, northerly, and vertical directions, respectively, whereas the corresponding values at the crest were 1.658, 1.474, and 0.843 g, respectively. The Pazarcık values were 0.064 and 0.215 g in the primary direction. The peak velocities, Arias intensities (Arias 1970), and significant durations (Trifunac and Brady 1975) are given in **Table 5**. The Elbistan abutment record had a peak velocity of 31 cm/s and a significant duration of 16 s, without the velocity pulses that Akinci et al. (2025) identified in eight Elbistan records, and the peak velocity at the station on the rupture was 164 cm/s. The crest-to-abutment ratio of the peak accelerations in the Elbistan event was 2.3 in the primary, 1.1 in the secondary, and 1.5 in the vertical direction. The abutment rock record is taken throughout as the motion imposed at the base of the dam, neglecting possible topographic amplification at the abutment and the spatial variation of the motion along the foundation, which a single rock station cannot resolve.

The primary PGA of 0.718 g exceeded the 0.45 g MCE input of the design analyses by a factor of 1.6, and the 0.18 g MDE by a factor of 4, whereas the crest PGA of 1.658 g remained below the 1.90 g computed for the MCE (Table 3). The Elbistan-to-Pazarcık ratio of the primary peak accelerations was 11 at the abutment and 7.7 at the crest; therefore, the second, near-field event governed the recorded dynamic demand.

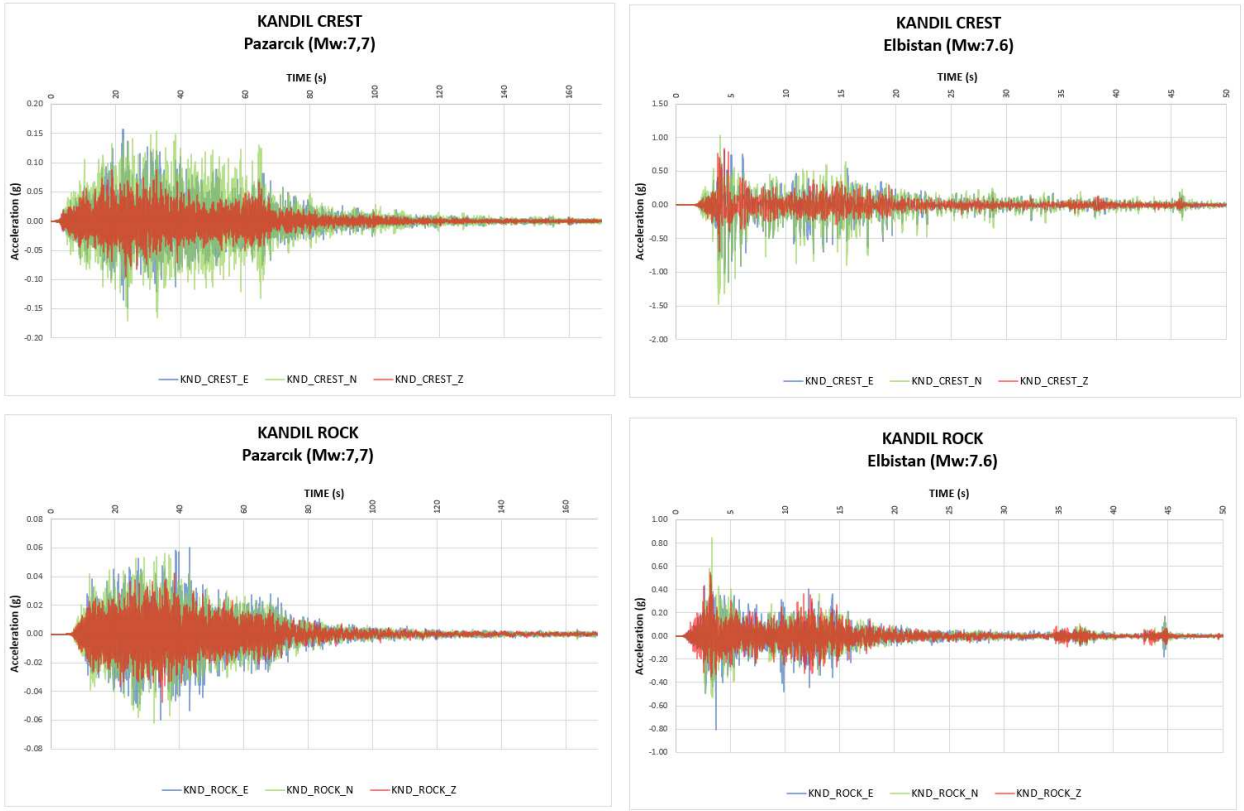


Fig. 5 Accelerograms recorded at Kandil Dam

5.2.Response spectra and amplification

Fig. 6 shows the 5% damped response spectra of the abutment and crest records in the primary direction, the design input, and the crest-to-abutment amplification as a ratio of the response spectra and the smoothed Fourier amplitude spectra (Konno and Ohmachi 1998); the derived quantities are summarized in Table 5. The Elbistan spectrum at the abutment had energy for short periods, with a mean period of 0.14 s; spectral accelerations of 0.98, 0.90, 0.39, and 0.25 g at 0.2, 0.3, 0.5, and 1.0 s, respectively; and ordinates up to 3.3 g below 0.1 s. The design input was the record of the Mw 6.3 Adana–Ceyhan earthquake of June 27, 1998, at the Ceyhan station (AFAD station 0105), a soil site with a V_{s30} of 263 m/s, which had peak accelerations of 0.28 and 0.23 g, peak velocities of 24 and 30 cm/s, and mean periods of 0.64 and 0.74 s in the east–west (EW) and

north–south (NS) directions, respectively, according to the processed record (Luzi et al. 2020). Both horizontal components scaled to the MCE PGA of 0.45 g are shown and bracket the design input (a 10 or 15 Hz low-pass filter, as in the design, changed the ordinates beyond 0.2 s by less than 3%), with the rock spectral shape of the Turkish earthquake code of the time (Ministry of Public Works and Settlement 2007), anchored at 0.45 g, as a reference (Text S1 in Online Resource 1). The recorded motion exceeded the scaled design input by a factor of approximately 4 at 0.1 s, 1.0–1.3 at 0.2 s, and 1.1–1.2 at 0.25 s. By contrast, it fell below the design input between 0.26 and 0.29 s, with a factor of 0.7–0.8 at 0.3 s, 0.3–0.5 at 0.34–0.44 s, and 0.3–0.5 at 0.5–1.0 s (2.1, 0.8, and approximately 0.5 against the code shape at 0.1, 0.3, and 0.5 s and beyond). Therefore, the exceedance was confined to periods that were shorter than approximately 0.3 s; at the periods of the dam, 0.24–0.44 s, the recorded demand was at most 1.2 times the scaled design input, and from 0.3 s onward, it was well below the scaled design input.

The amplification function identified the fundamental period T_1 of the dam as 0.34 s under weak Pazarcık motion, which is within 4% of the 0.355 s of the design model, with a crest-to-abutment Fourier amplification of 16 at that period. Under the strong Elbistan motion, the peak shifted to 0.44 s in the primary direction, and the amplification at the peak decreased to 9. The northerly component peaked at 0.51 s in the strong event, not necessarily the same mode, and was not combined with the primary-direction value. Away from the fundamental period, the amplification of the Elbistan motion was only 1–2.6 at periods shorter than 0.1 s, and it decreases from 2 at 1 s to approximately unity beyond 2 s. This explains why the crest PGA, dominated by short-period energy, was only amplified by a factor of 2.3, whereas the spectral acceleration at T_1 increased from 0.40 g at the abutment to 2.0 g at the crest. The half-power bandwidth of the transfer function gave an equivalent damping of approximately 10% for the Pazarcık event, and an upper bound of

20–30% for the Elbistan event, whose broad peak overlapped the pre-event mode (Text S1 in Online Resource 1).

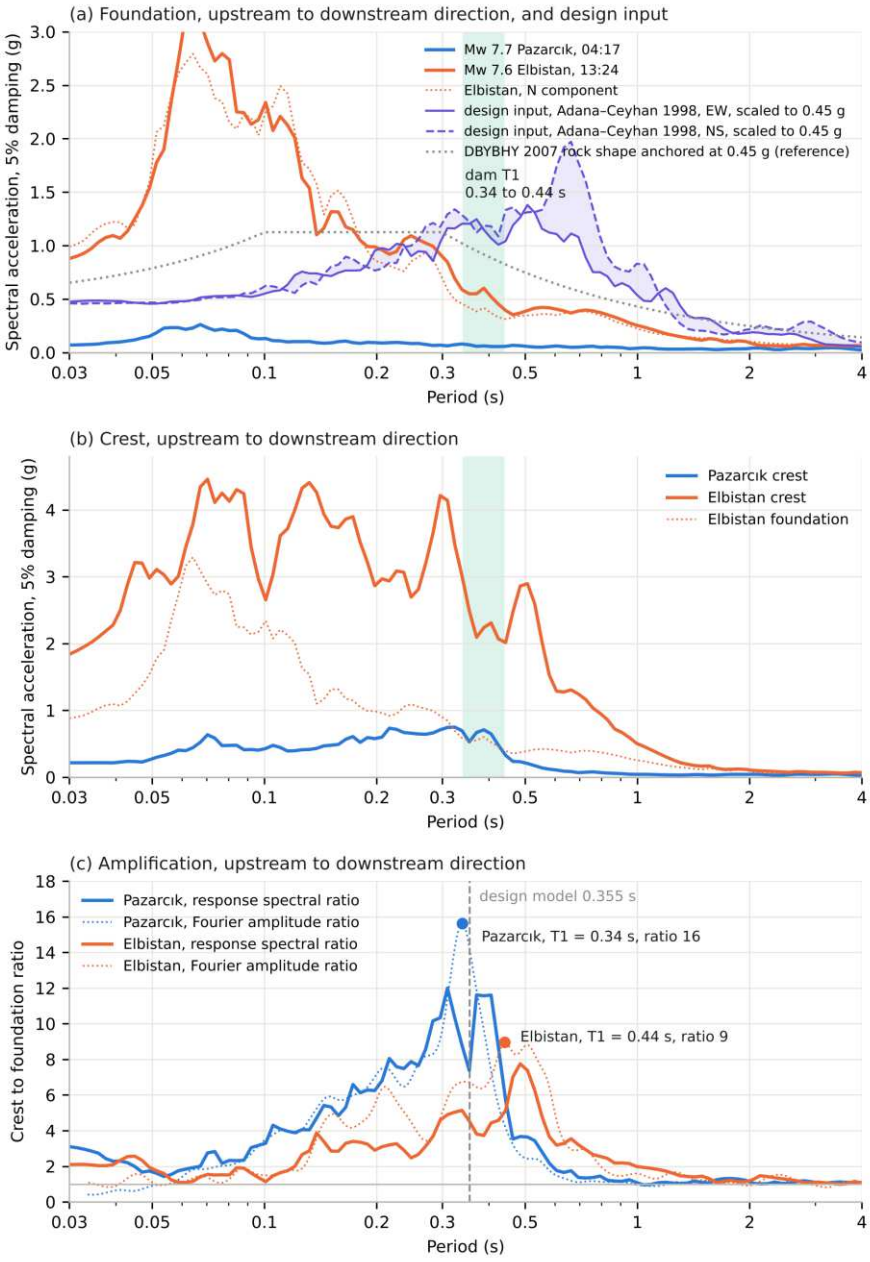


Fig. 6 Response spectra and amplification from the foundation and crest accelerograms for February 6, 2023, upstream-to-downstream direction. (a) Foundation, with the design input, the EW and NS components of the 1998 Adana–Ceyhan record (AFAD station 0105; Luzi et al. 2020) each scaled to the MCE PGA of 0.45 g (shaded between them), and the rock spectral shape of DBYBHY 2007 anchored at 0.45 g as a reference. (b) Crest. (c) Crest-to-foundation amplification

as the ratio of the 5% damped response spectra (solid) and of the smoothed Fourier amplitude spectra (dotted), with the fundamental period of the design model

5.3.Strain-compatible stiffness check

The period elongation from 0.34 to 0.44 s between the weak and strong events implies that, for a shear beam with unchanged modal mass and mode identification, an effective modal stiffness ratio is

$$\frac{G_{\mathrm{strong}}}{G_{\mathrm{weak}}} = \left(\frac{T_{1,\mathrm{weak}}}{T_{1,\mathrm{strong}}}\right)^2 = (0.34/0.44)^2 = 0.60 \quad (1)$$

The ratio of 0.60 is a first-order estimate of a stiffness reduction of approximately 40%, not a measurement of the material modulus. **Fig. 7** examines whether the strain induced in the dam is consistent with this reduction. Double integration of the crest and abutment records after alignment of their time bases, with the displacements band-pass filtered between 0.2 and 8 Hz, gives a peak relative displacement of 7.3 cm during the Elbistan event, that is an apparent average shear strain of 0.07% over the 103-m height and an effective strain of 0.046% with the factor of 0.65 of the equivalent linear convention (Seed and Idriss 1971). This is a global deformation measure, not a local shear strain, because the reference sensor is on the abutment and the relative displacement includes any spatial variation in the foundation motion, rocking, and three-dimensional deformation. The corresponding Pazarcık values are 3 cm and 0.02 to 0.03%. For mean effective confining stresses of 400 to 1000 kPa, representative of the central third of the embankment, the modulus reduction curves reported by Menq (2003) for gravels take the form

$$\frac{G}{G_{\max}} = \frac{1}{1 + \left(\frac{\gamma}{\gamma_{\mathrm{r}}}\right)^{a}} \quad (2)$$

299 with the reference strain γ_r and exponent a depending on the coefficient of uniformity and
300 confining stress (Text S1 in Online Resource 1). For coefficients of uniformity between 10 and 50,
301 the range of compacted rockfill, consistent with the gravel data of Rollins et al. (1998), gives a
302 G/G_{max} of 0.25–0.65 at the Elbistan strain and 0.45–0.95 at the Pazarcık strain, and a ratio of 0.45–
303 0.70 for matched gradation that brackets the period-based 0.60.

304 The design modulus, $K_{2max} = 150$ in the formulation by Seed and Idriss (1970), gives a small-strain
305 shear modulus of approximately 870 MPa and a shear wave velocity of approximately 640 m/s at
306 700 kPa, and the uniform shear beam period of $2.61H/V_s$ (Gazetas 1987) is 0.42 s, in the measured
307 range of 0.34–0.44 s. The agreement of one modal period does not validate the damping,
308 constitutive behavior, or permanent deformation and joint stress predictions of the model, and no
309 post-event weak-motion window exists from which stiffness recovery could be established. The
310 defensible reading is that the response to an abutment motion of 0.718 g exhibited strain-dependent
311 softening of the order of 40% with equivalent damping rising from 10% to an upper bound of 20–
312 30%, which the design model, an elastic perfectly plastic model with strain-independent moduli
313 below yield, did not represent, and that neither the global strain of 0.07% nor the surface
314 observations show the large-scale instability that strength loss, pore pressure build-up, or deep-
315 seated sliding would have produced.

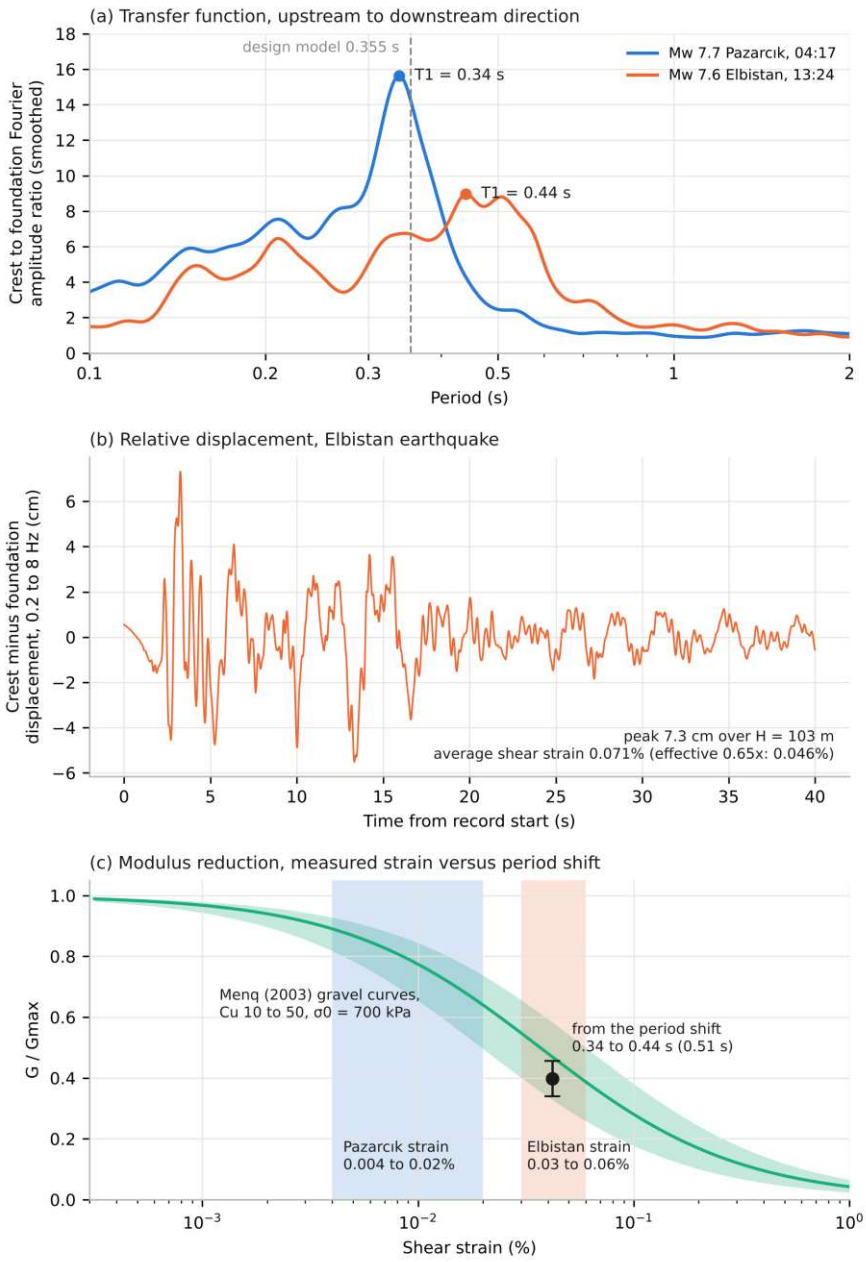


Fig. 7 Dynamic characteristics of Kandil Dam from the records of February 6, 2023. (a) Crest-to-foundation Fourier amplitude ratio in the upstream-to-downstream direction with the fundamental periods of the two events and of the design model. (b) Relative displacement between the crest and foundation during the Elbistan earthquake from double integration of the records, 0.2 to 8 Hz. (c) Modulus reduction curves from Menq (2003) for gravels at a confining stress of 700 kPa with the strain ranges of the two events and modulus ratio implied by the period shift

5.4.Permanent displacement check

The permanent displacements measured by the surface survey are the primary evidence for the deformation mechanism, and the sliding block calculations test their consistency with the recorded motions. **Fig. 8** shows the displacement vectors of the 22 surface points and 12 parapet points between the surveys of August 4, 2022, and February 8, 2023, in the dam axis system (**Table S9** in Online Resource 1). The deformation in the preceding nine years amounted to a few centimeters; therefore, the change over this six-month interval was attributed to the earthquake sequence. The whole downstream shell moved downstream, and the movement decayed with depth, from 25–39 cm along the crest edge and the berm at El. 1076 m in the central and right-of-center sections (4–13 cm toward the left abutment) to 5–11 cm at El. 1060 m and 5–7 cm at El. 1031 m. Moreover, the parapet wall moved by 2.5–7.6 cm and settled by up to 6 cm. Point SF12, the 39 cm maximum, is located on the berm 25 m below the crest, and in the central and right-of-center sections, the displacement at the top of the profile exceeded that at El. 1060 m, 39 m lower, by 60 to 80% of its value. This places most of the deformation, if it is read as shear deformation, in the upper 40 m of the shell, where the confining stress was lowest and the amplification highest. The crest edge points, on the downstream slope 12.5–13.6 m from the parapet line, moved 20–30 cm more than those on the parapet. This extension belongs to the same deformation as the longitudinal cracking, guardrail displacement, and parapet joint openings, which are discussed in Section 6.1, and it was accommodated by distributed strain, the opening of several fissures, and the settlement of the downstream shoulder; thus, the widest single crack was less than 10 mm wide. The surface measurements did not identify an internal shear zone, and the pattern combined distributed shear, densification, and distortion of the shoulder in proportions that the back analysis will resolve. A movement of 3–12 cm toward the left abutment shared by nearly all points and an apparent heave

of 2–4 cm at the lowest row were attributed to a small datum shift of the reference pillars, which did not affect the shape of the downstream profile.

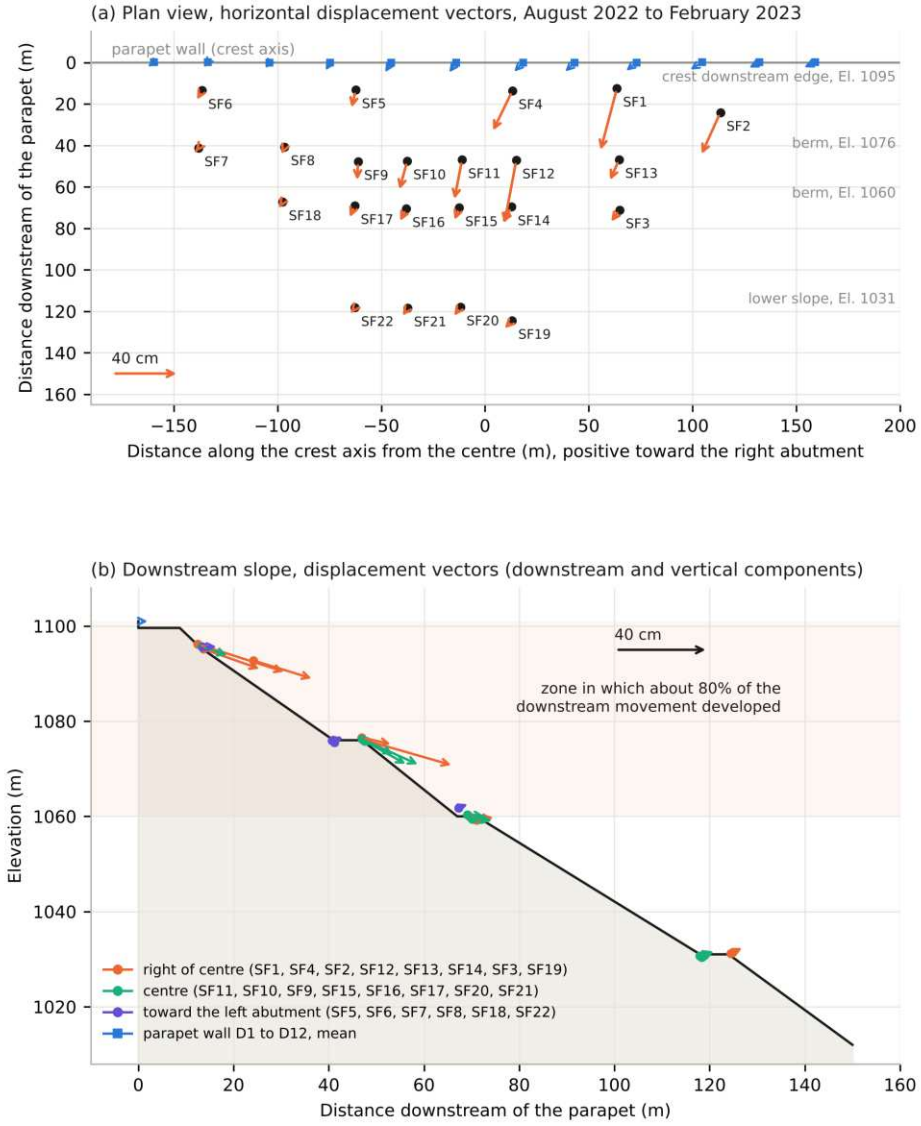


Fig. 8 Permanent displacements between the surveys on August 2022 and February 2023 in the dam axis system. (a) Plan view of the horizontal displacement vectors of the surface points (black) and parapet points (blue). (b) Section of the downstream slope with the vectors of the downstream and vertical components; colors distinguish the central, right-of-center, and left sections, and the shaded band marks the zone in which approximately 80% of the downstream movement developed

The sliding block calculations (**Table 6**) compare this pattern with the recorded motions. The rigid block described by Newmark (1965) accelerates relative to the ground, whereas the ground acceleration $a(t)$ exceeds the yield value, and the yield coefficient k_y of a block on the downstream slope follows from the friction angle φ and the slope angle β,

$$\ddot{u}(t) = a(t) - k_y g \text{ for } a(t) > k_y g, k_y = \tan(\varphi - \beta) \quad (3)$$

with one-directional sliding (integration convention and sensitivity cases in Text S1 in Online Resource 1). For the deep critical surface of the design, integration of the abutment record in the primary direction gives 2–3 cm at a yield coefficient of 0.21, and approximately 2 cm at a yield coefficient of 0.235. The abutment record is a conservative proxy for the average acceleration of a full-height mass, which Makdisi and Seed (1978) set to approximately 0.35 of the crest value, which gives 1 cm or less. The procedure proposed by Bray and Travasarou (2007) for a flexible full-height mass with an initial period of 0.34 s ($2.6H/V_s$, the fundamental period of the dam), a spectral acceleration of 0.40 g at 1.5 times that period, and Mw 7.6 at $k_y = 0.21$ gives a probability of 40% that the displacement is negligible (1 cm or less) and, conditional on a larger value, a median of 2.6 cm. Its rigid form, driven by a PGA of 0.718 g, gives 17 cm, which is an overestimate for a 100-m mass because the mean period of the near-field motion is 0.14 s. The value of 21 cm in the design analysis is the permanent crest displacement of a continuum model, not the displacement of a sliding surface (Table 3).

For the upper shell, the block is driven by the crest record reduced to the average acceleration of the mass, 0.8 of the crest value for a mass extending to 0.25 times the height and 0.65 for a mass extending to 0.4 times the height (Makdisi and Seed 1978). This simplification scales every ordinate alike, with a yield coefficient of 0.20–0.30 from friction angles of 46°–52° at normal stresses of 50–150 kPa for the zone (Leps 1970) on the 1.4H to 1V slope. Downstream sliding

occurs when the ground accelerates toward the reservoir. This gives 10–32 cm for a mass extending to 0.25 times the height and 4–15 cm for the deeper mass (0.4 times the height) over the range of k_y. The polarity opposite that of the record gives 27–55 and 13–32 cm, and the vertical crest record in the yield resistance changes the values by less than 10%. Against the measured 25–39 cm, the rigid block reproduces the order of magnitude of the upper shell movement only for the shallowest mass and the lower end of the strength range, and it underpredicts it for a mass extending to 40 m. Therefore, the calculations exclude the movement of the deep surface under the recorded motion and make deformation confined to the upper shell under the amplified crest motion the plausible mechanism. However, the rigid block does not reproduce the measured pattern by itself. The decay with depth is more consistent with distributed shear strain accumulated over the upper shell, together with the settlement of the downstream shoulder, than with sliding on a single surface, an important distinction for the planned three-dimensional back analysis.

6. Observed Performance

6.1. Overall condition and damage classification

Visual inspections and the monitoring and seepage data confirmed that Kandil Dam and its appurtenant structures sustained no damage that compromised reservoir safety or power generation, which resumed within 6 h of the first earthquake and continued after the second, when the reservoir was drawn down through the turbines (Section 6.5). The settlement of the parapet wall was 6 cm, 0.06% of the dam height, and that of the downstream crest edge was 8–12 cm, up to 0.12% of the dam height. The maximum longitudinal crack width was less than 10 mm. In the classification system by Pells and Fell (2002), the crack width falls in class 0 and the settlement falls in class 1, where the more severe indicator represents minor damage (**Table 7**). In the crest

settlement ratio against PGA compiled by Swaisgood (2014), the dam falls in the range of minor deformation (**Fig. 9**). **Table 8** compares each recorded parameter with its expectation. Except for the downstream displacement of the upper shell (Section 5.4), the observed response remained below the design predictions.

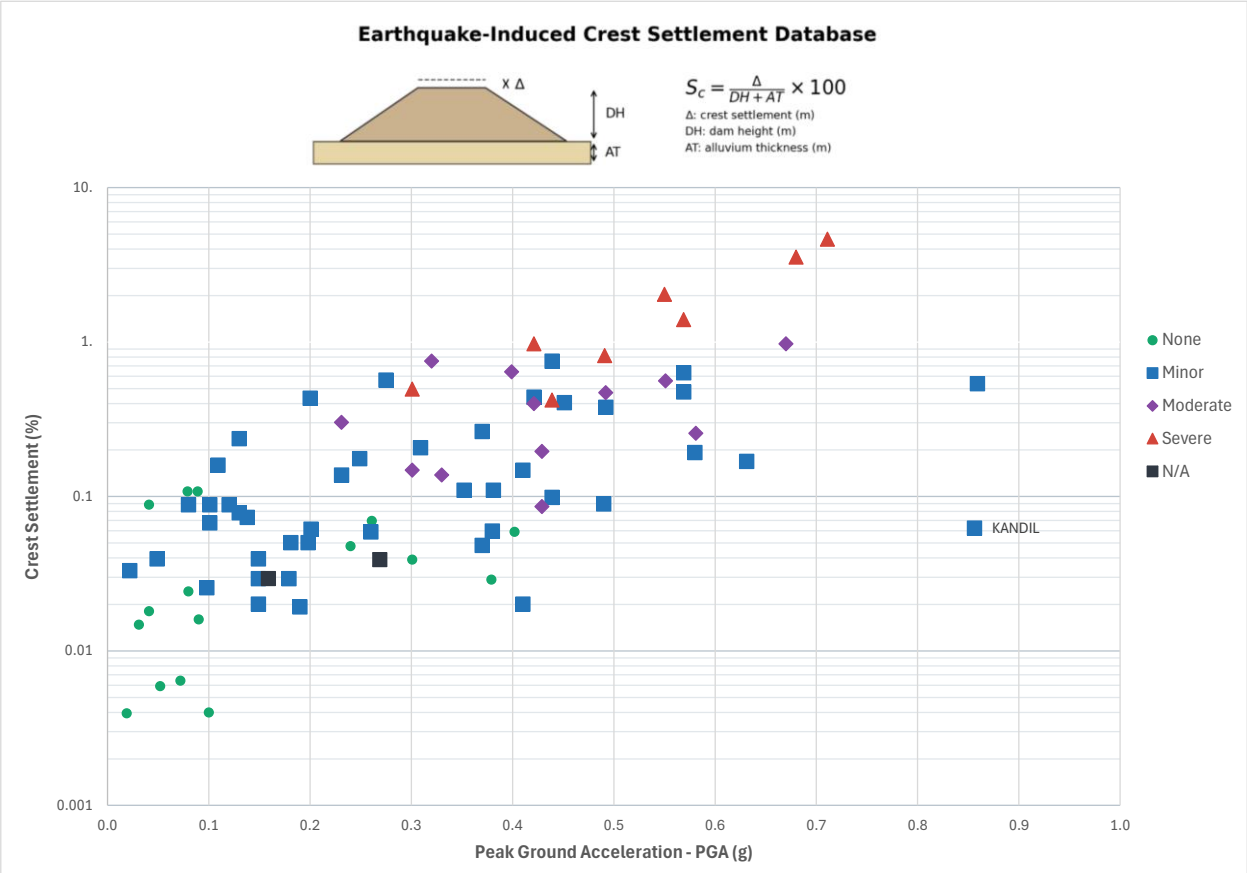


Fig. 9 Earthquake damage as function of crest settlement based on Swaisgood (2014)

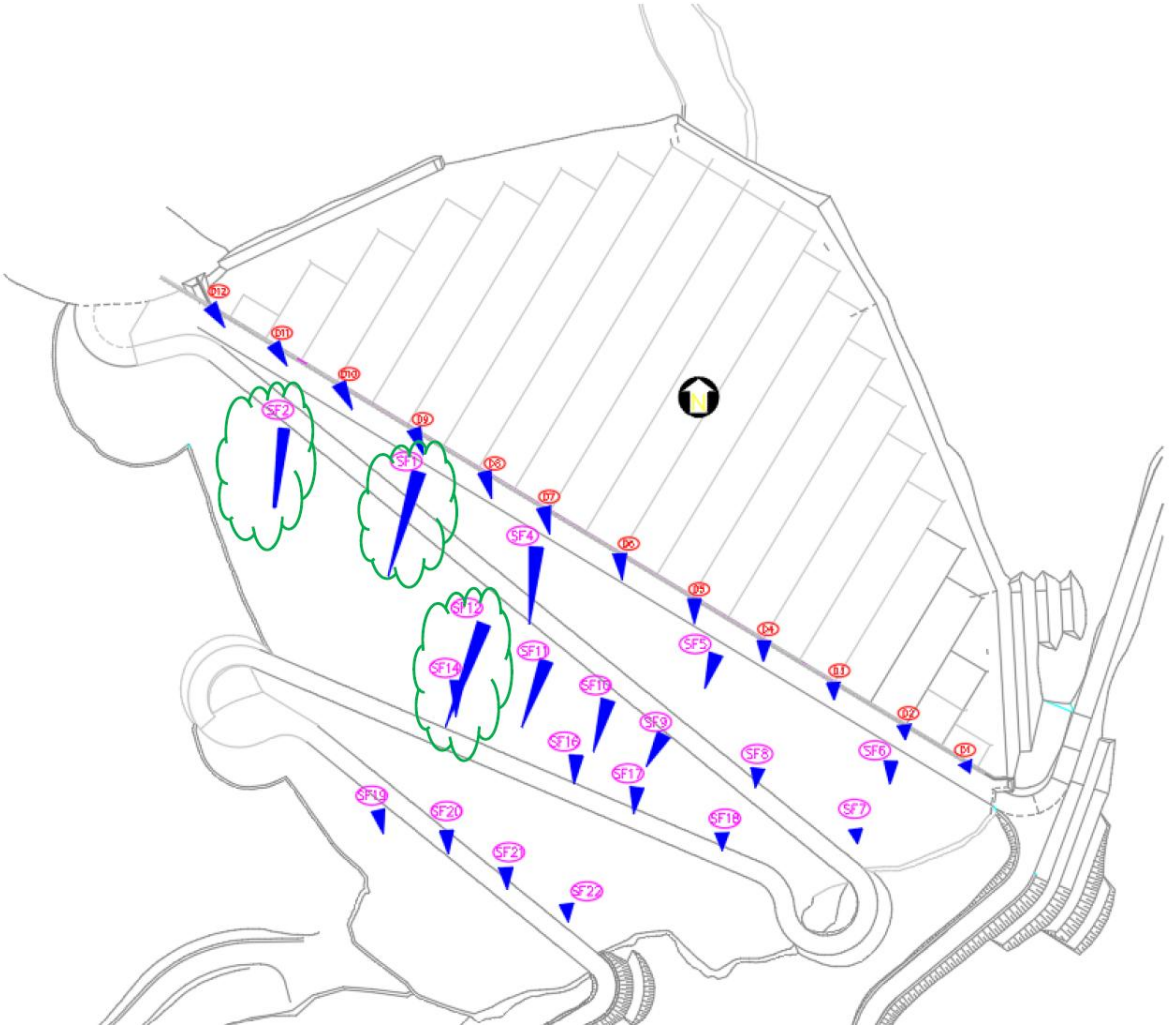
Visual inspections identified rockfalls on the right abutment slopes (**Fig. S6** in Online Resource 1), deformation and guardrail movements in the downstream crest area (**Fig. 10**), cracks in the joint fillers above the reservoir level, and openings in the expansion joints of the parapet walls. Several of the PVC covers of the waterstops were cut or separated from their fixings, and the submerged face was inspected with an ROV on March 2, 2023 (Section 6.6).



Fig. 10 Crack observed on the crest

6.2.Deformation

Three-dimensional displacements are monitored at topographic points on the crest, parapet wall, and downstream rockfill. The earthquake-related pattern was 25–39 cm downstream at the crest edge and the upper berm, and decayed to 5–7 cm at the lower slope, as described in Section 5.4 and **Figs. 8 and 11**. The settlement was 6 cm at the parapet and 8–12 cm at the crest edge and upper berm. No increase in seepage or face slab damage accompanied these movements.



423

424 **Fig. 11** Locations of surface measurements and movement directions

425

426 The 29 hydraulic settlement cells (**Fig. 12**), except the six cells with drifted baselines (SC1, SC2,
427 SC3, SC7, SC18, and SC29) and four cells near the right abutment, showed an approximately
428 uniform change of 10–13 cm across all the elevations and sections within three days of the events.
429 Regardless of the depth, the cells showed signatures of a shift in the readout datum, rather than
430 differential settlement of the fill. This is consistent with the 11 cm settlement that the survey
431 measured at the upper berm; therefore, the cells did not resolve the internal settlement distribution,
432 and the earthquake-related settlement was taken from the survey. The electro-level devices on the

face detected slight tilting at ECL-3 and ECL-11, which subsequently reverted, indicating no permanent change in the face geometry. The tilt during the shaking was not recorded.

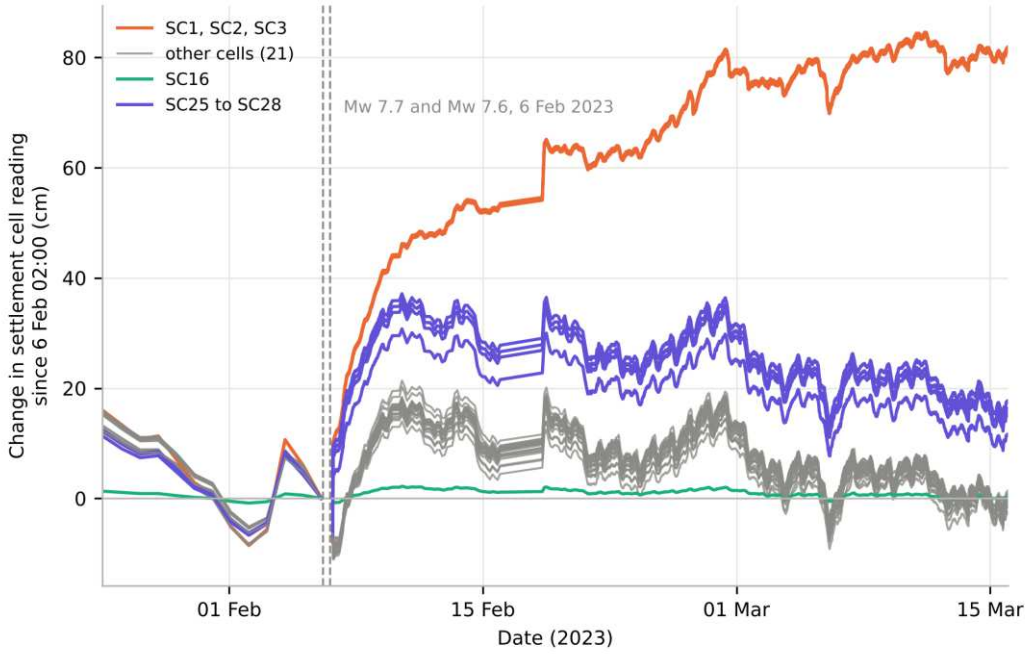
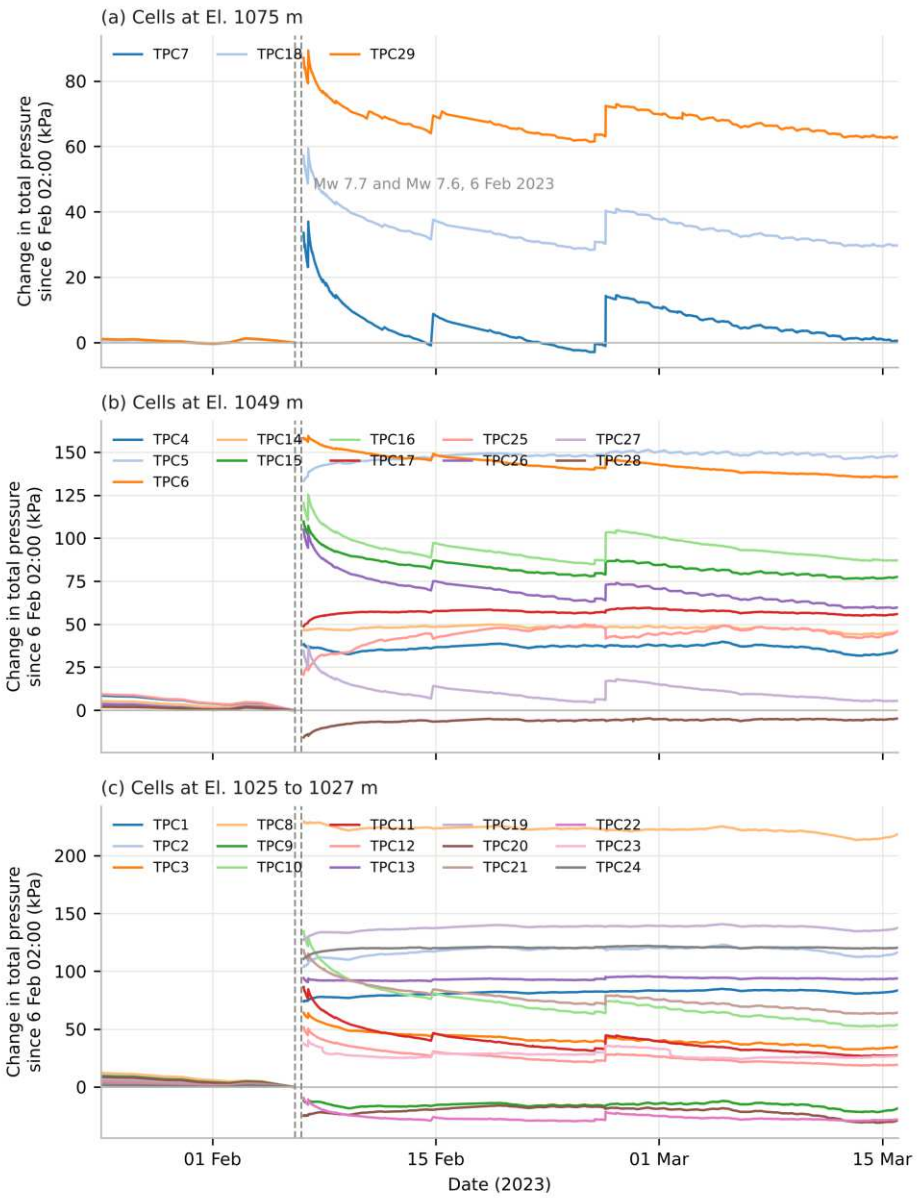


Fig. 12 Change in the readings of the 29 hydraulic settlement cells since 02:00 on February 6, 2023. The six cells with drifted baselines and four cells near the right abutment are distinguished. The near-uniform change in the remaining cells was attributed to a shift in the readout datum

6.3. Total pressures and foundation pore pressures

The 29 TPCs are installed in the rockfill at elevations of 1025, 1049, and 1075 m in the three instrumented sections. All but four of the cells recorded a step increase in the total pressure that was complete at the first post-event reading, with a mean of 75 kPa and a maximum of 229 kPa at TPC8 (**Fig. 13**). The steps persisted or relaxed over weeks, indicating that the stress in the fill was redistributed by densification.



446

447 **Fig. 13** Change in the total pressure recorded by the 29 TPCs since 02:00 on February 6, 2023, by
448 installation elevation. The logger recorded no readings between 02:00 and 17:10 on February 6,
449 2023.

450 The foundation and abutments contain 12 VWPs (**Fig. 14**). VWP1, VWP2, and VWP3 lie at
451 elevations of 990, 970, and 950 m, respectively, 8–48 m below the plinth, in one borehole at the
452 plinth of section 0+175. VWP8 lies at an elevation of 990 m near section 0+240. Their heads stand
453 30–45 m below the reservoir level, and they measure the confined pressure in the rock below the
454 plinth, which carries the grout curtain. The different residuals of VWP2 and VWP3 after the events

indicate that the sensor levels in the shared borehole responded as distinct units, as the seals between the sensor levels were intended to ensure. The responses are summarized in **Fig. 15** and **Table 9**, with the excess head measured relative to the pre-event regression of each head on the reservoir level, and the decay fitted by exponential plus constant functions (fit intervals and residuals in Text S1 in Online Resource 1). At the first reading after the events, the excess head was 7.9, 14.2, 16.7, and 5.3 m at VWP1, VWP2, VWP3, and VWP8, respectively, and the fits extrapolated to the Elbistan earthquake give model-dependent peaks of approximately 9, 15–16, 18–22, and 7 m, respectively, that is 0.7–2.1 bar. This is based on the assumption that the rise began with the Elbistan earthquake, which produced eleven times the abutment acceleration of the first, and that the decay was exponential from the onset. The coseismic peak itself was not observed, and the contribution of the first earthquake cannot be separated. The excess decayed with e-folding times of 10–19 h. VWP3 returned to its pre-event relation within 2 d, whereas VWP1, VWP2, and VWP8 retained residuals of 1.9, 6.5, and 1.3 m after six weeks. The piezometers in hydraulic contact with the reservoir changed by 2 m or less, and the sensor temperatures did not change.

Three interpretations were examined, and the data constrain them without excluding them. The undrained response of the rock to a local total stress change (Skempton 1954) cannot be tested directly, because the nearest total pressure cells lie in the fill 72–114 m from the piezometers and the weight of the dam, unchanged in total, may have been redistributed locally. However, the data show that the response increased with depth, that the rise exceeded the nearest stress step at VWP2 and VWP3, and that the pulse decayed over hours, whereas the stress steps persisted for weeks; therefore, stress redistribution alone does not account for the observation. A short inflow of reservoir water through the face or its joints is unlikely, because the piezometers in contact with

478 the reservoir barely moved, the confined deep piezometers moved most, and the seepage discharge
479 did not change (Section 6.5). The pattern in space and time is most consistent with a coseismic
480 change in the pore pressure in the jointed foundation rock generated by the static and dynamic
481 strain of the Mw 7.6 rupture 3 km away, followed by recovery through pressure diffusion. This
482 response was described by Wang and Manga (2021) for confined aquifers within approximately
483 one rupture length of the fault, and was illustrated by the recovery of wells near the Koyna and
484 Warna reservoirs over a month (Ramana et al. 2007). A poroelastic response and a mechanically
485 induced change are not mutually exclusive. If the depth z of each sensor below the plinth is taken
486 as the drainage length, an assumption that lateral drainage through the fractured rock would
487 invalidate, then the hydraulic diffusivity follows from the half-time t_{50} of the transient part of the
488 excess head. That is,

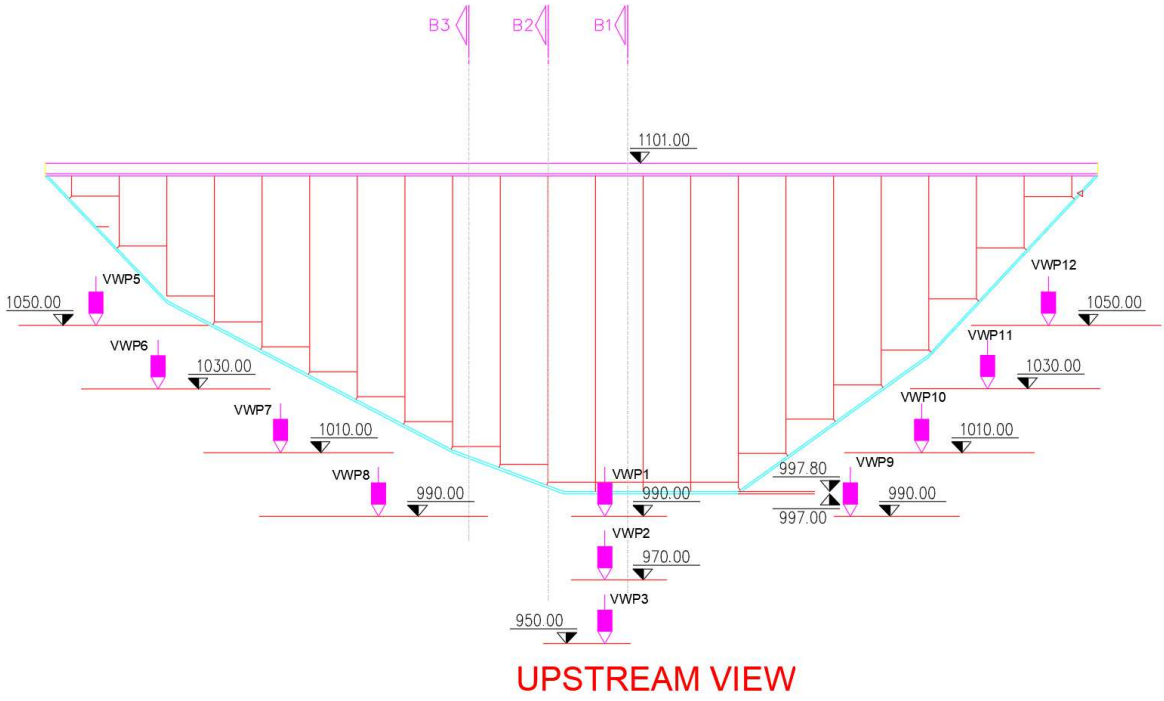
489 $$D = \frac{z^2}{0.91\, t_{50}} \tag{4}$$

490 which gives 1×10^{-3} to 5×10^{-2} m^2/s for half-lives of 0.4–0.6 d and, for a specific storage of 10^{-6}
491 to 10^{-5} m^{-1}, conductivities of the order of 0.01 to 4 Lugeon. These are illustrative values that scale
492 with the square of the assumed drainage length.

493 The residual offsets, largest at VWP2, are consistent with a small permanent change in the
494 conductivity of the fractured rock near the grout curtain, although a persistent offset does not by
495 itself demonstrate one. Such changes have been documented in fractured rock at peak dynamic
496 stresses of 0.02–0.21 MPa, with recovery over months and persistent steps attributed to localized
497 changes near the well (Elkhoury et al. 2006; Manga et al. 2012; Candela et al. 2014). By contrast,
498 the abutment rock at Kandil Dam experienced a dynamic shear stress of approximately 1–2 MPa,
499 an order of magnitude higher. The piezometric heads below the plinth remained 20–40 m below
500 the reservoir level throughout; the piezometers did not measure the uplift at the plinth contact, and

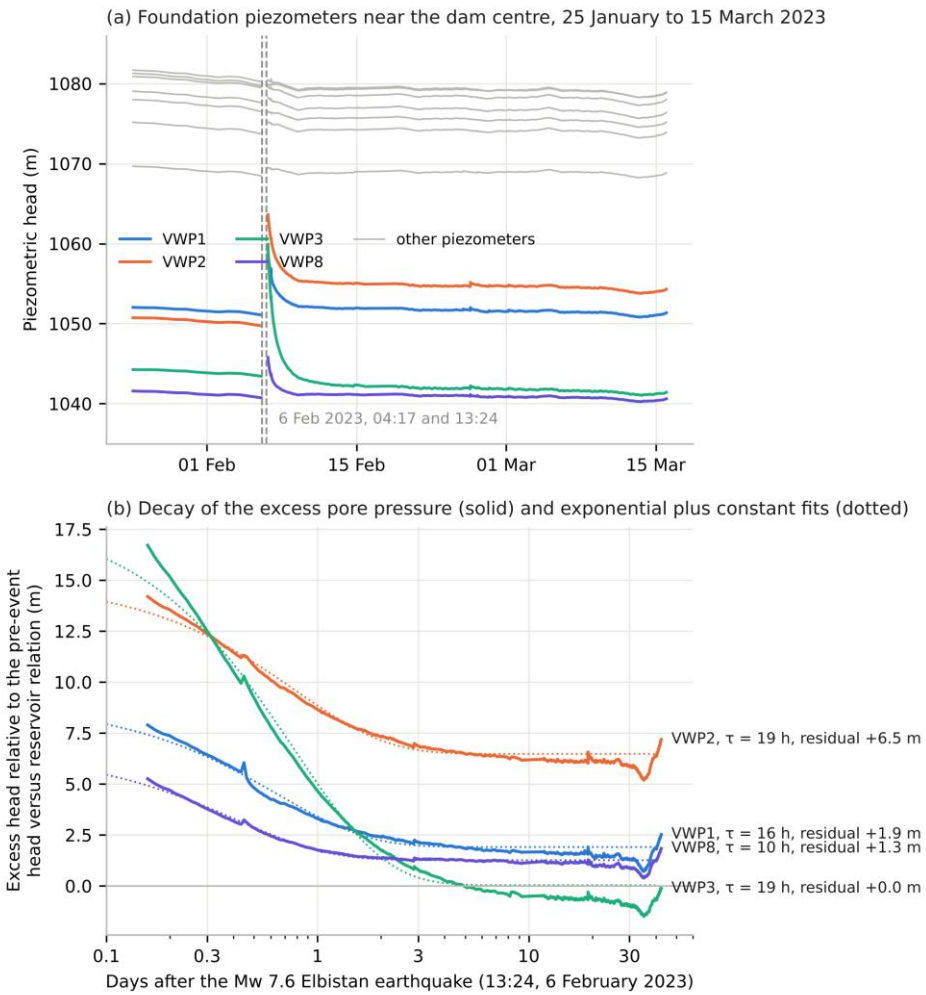
501 the effect of the residual at VWP2 on the plinth and the grout curtain is a quantity of interest in the

502 planned back analysis.



503

504 **Fig. 14** Locations of the VWPs



505

506 **Fig. 15** Pore pressure response of the foundation piezometers near the dam center. (a) Piezometric
507 heads from January 25 to March 15, 2023, with the two earthquakes marked. The logger recorded
508 no readings between 02:00 and 17:10 on February 6, 2023. (b) Excess head relative to the pre-
509 event head versus reservoir relation against time after the Elbistan earthquake, with exponential
510 plus constant fits

511

512 ***6.4. Face slab joints, stresses, and temperature***

513 Five of the 12 HJMs on the face and most of the components of the 11 three-dimensional plinth
514 joint meters were operational, and they were read at 02:00 and 17:10 on February 6, 2023.
515 Therefore, their changes are residual values, and the transient maxima are unknown. The residual
516 changes included a maximum closure of 3 mm at HJM7 and maximum openings of 6 mm at

PJMZ9 and PJMY9, against peak dynamic movements of up to 15.6 mm, which were computed for the MCE (Table 3), a one-sided comparison, because a residual below the peak prediction does not show the transient value. The cumulative record since impounding (**Fig. 16**) shows that 36–63% of the total movement developed during the initial impounding, and that 86–100% had developed before the earthquakes, except at HJM7, which was 49%. The cumulative opening of approximately 38 mm at HJM2 exceeded the design total; however, it remained well within the 160 mm expansion capacity of the copper waterstop and far below movements above 70 mm, with 46 mm of shear considered capable of shearing copper waterstops at the 145-m-high Mohale CFRD (Johannesson and Tohlang 2007), without any change in the seepage record.

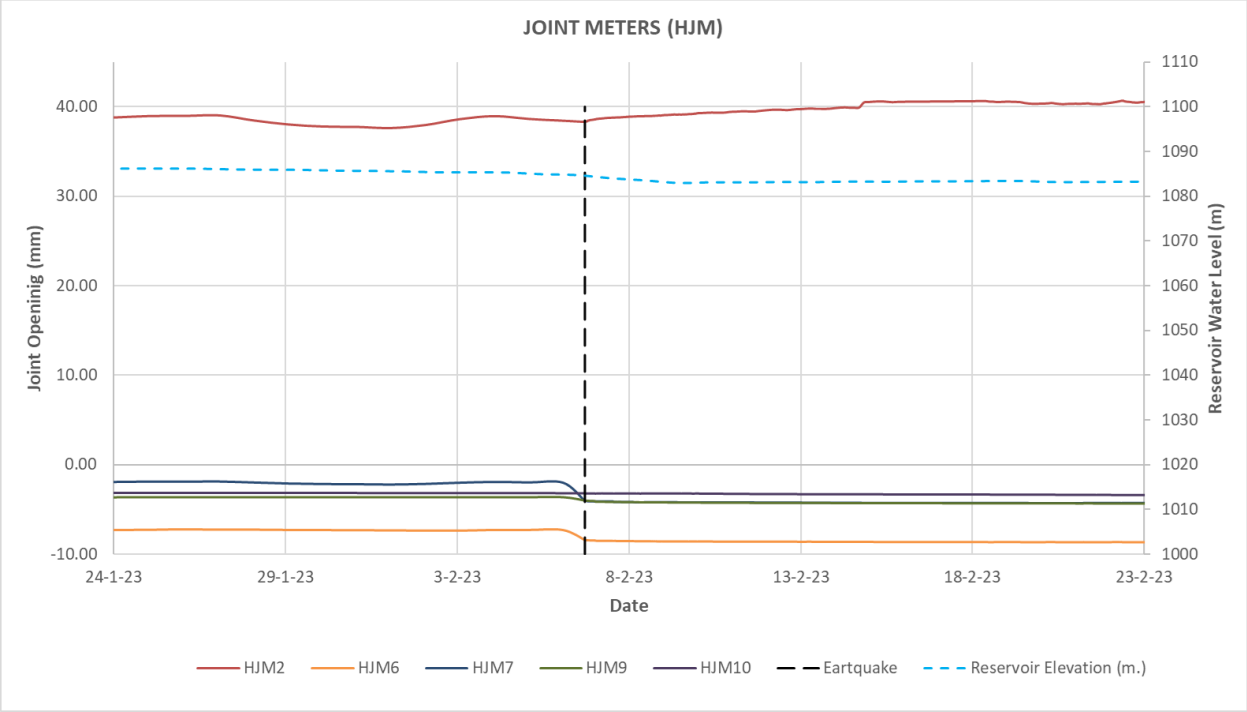


Fig. 16 Values recorded by the HJMs

The strain gauge components on the face with continuous readings included 19 channels, of which 17 were classed as fully operational in the instrument inventory (Table S8 in Online Resource 1). Between 02:00 and 17:10, they recorded a maximum increase in compressive stress of 3.1 MPa at

SGY11 and a maximum compressive stress of 12 MPa at SGY12, with a concrete modulus of 32,000 MPa applied to the strains (**Fig. 17**). These are residual values at sampled times and do not demonstrate that the transient stress remained below the computed MCE of 14.5 MPa. They show that no residual stress approached the 30 MPa characteristic strength, and that the strains remained within the elastic range at the instrumented locations. Among the 32 temperature sensors on the face and the plinth, only TS26 showed a deviation, with a drop of 2 °C that recovered within 3 d, suggesting a temporary gap in the joint sealing that was filled by fly ash from the cover.

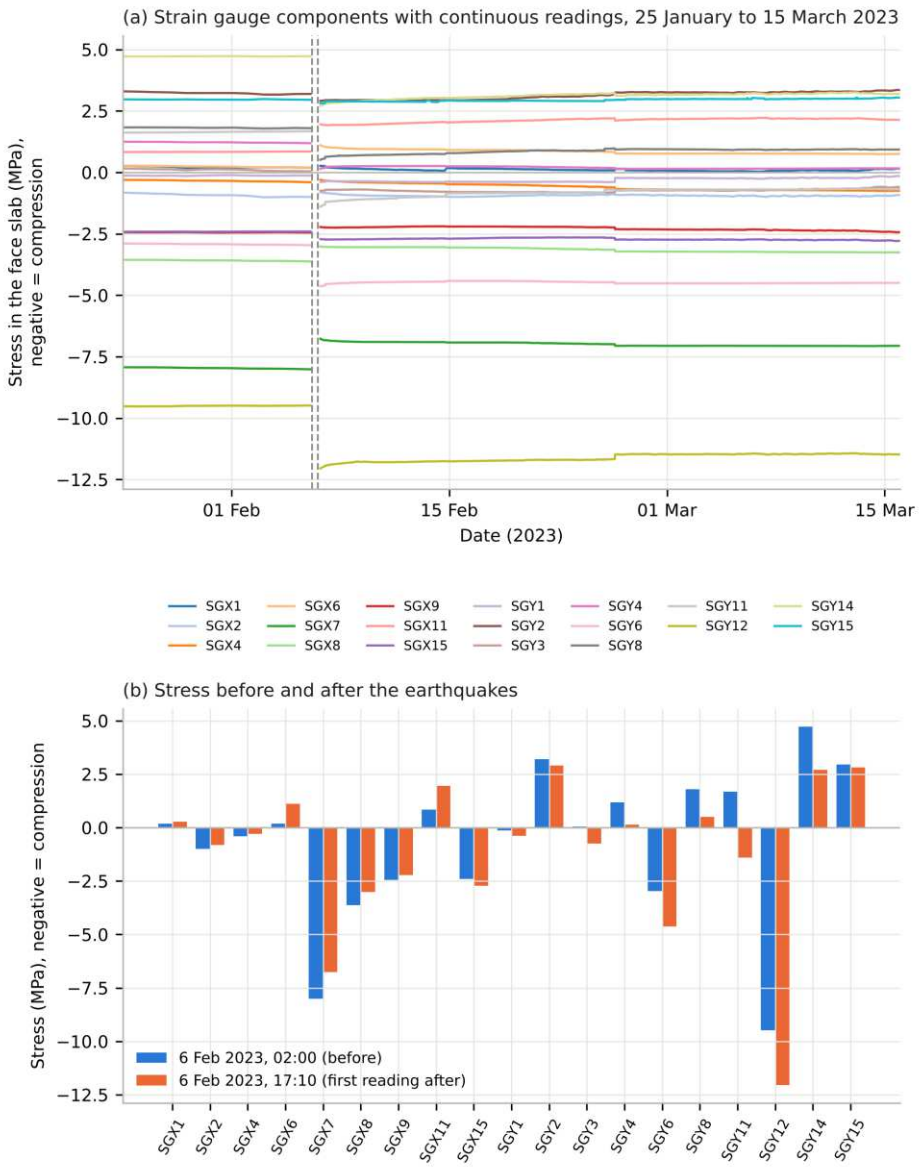
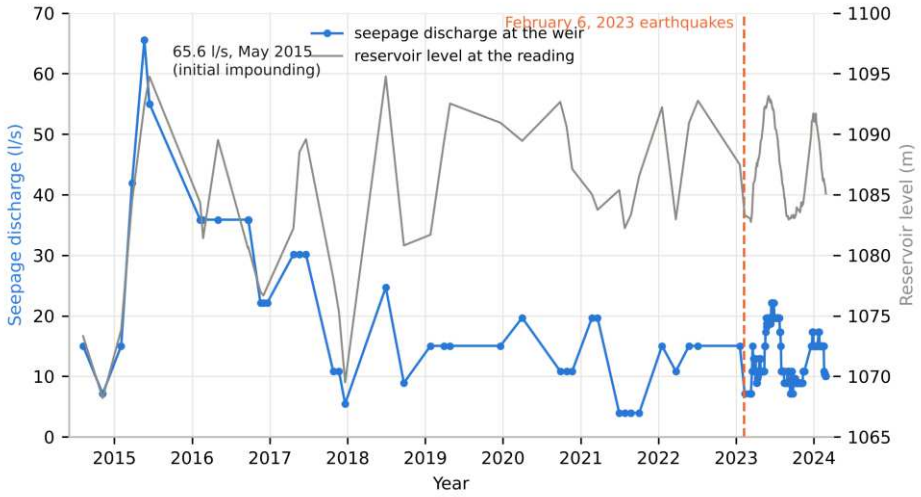


Fig. 17 Face slab stresses from the strain gauge components with continuous readings, with a concrete modulus of 32,000 MPa applied to the measured strains. (a) Time series from January 25 to March 15, 2023. (b) Values at 02:00 and 17:10 on February 6, 2023

6.5.Seepage and reservoir level

Seepage from the dam body, foundation, and abutments is collected at a V-notch weir at the downstream toe (**Fig. S7** in Online Resource 1), where the discharge and clarity are recorded. Leakage through a CFRD depends on the reservoir level (Jia et al. 2016); therefore, the readings

548 were compared at similar levels. On January 18, 2023, the discharge was 15 L/s at a reservoir level
549 of 1087 m and on February 10, 2023, the first reading after the earthquakes, it was 7 L/s at 1083
550 m, and the water remained clear (**Fig. 18**). As the reservoir level increased to 1092–1093 m in May
551 and June 2023, the discharge reached 15–22 L/s, compared with 11–15 L/s at the same levels in
552 2019–2022 and 30–36 L/s in 2016–2017. The difference from 2019 to 2022, approximately 1 cm
553 of head on the weir, coincided with the spring high-flow season of the abutment inflows, and it did
554 not persist. The readings from July 2023 to February 2024 fell back within the band of 2020 to
555 2022. The weir is read manually with a head resolution of 0.5 cm, 2–3 L/s in this range, and no
556 readings exist for the first four days; therefore, an early transient increase of the kind recorded at
557 Minase Dam in 1964 (ICOLD 2010) or Zipingpu Dam in 2008 (Guan 2009) cannot be excluded.
558 However, the record establishes that no sustained increase relative to the historical behavior was
559 detected, and that the seepage remained below the initial leakage reported for most CFRDs (**Table**
560 **S10** in Online Resource 1).



561

562 **Fig. 18** Seepage discharge at the V-notch weir between August 2014 and February 2024, with
563 the reservoir level at each reading. The vertical line marks the date of the earthquakes, February
564 6, 2023

The automated level gauge on the upstream face, logged at 1-min intervals, recorded fluctuations of up to ±1 m that persisted for approximately 30 min after the Elbistan earthquake and decayed from ±0.8 to ±0.2 m (**Fig. 19**a). Their persistence after the shaking identifies them as surface oscillations of the reservoir rather than a sensor response. The reservoir stood at 1084.5 m, 12.5 m below the normal maximum level of 1097.0 m. The fill crest at El. 1099.0 m was 0.45 m above the flood level of 1098.55 m, and the dependable freeboard was provided by the parapet wall at El. 1101.0 m, which was designed as the water-retaining element against waves and the design flood (Hidro Dizayn 2009). After the events, the reservoir was drawn down to 1083 m through the turbines while the safety of the dam was confirmed, and refilling was allowed after March 14, 2023 (Fig. 19b).

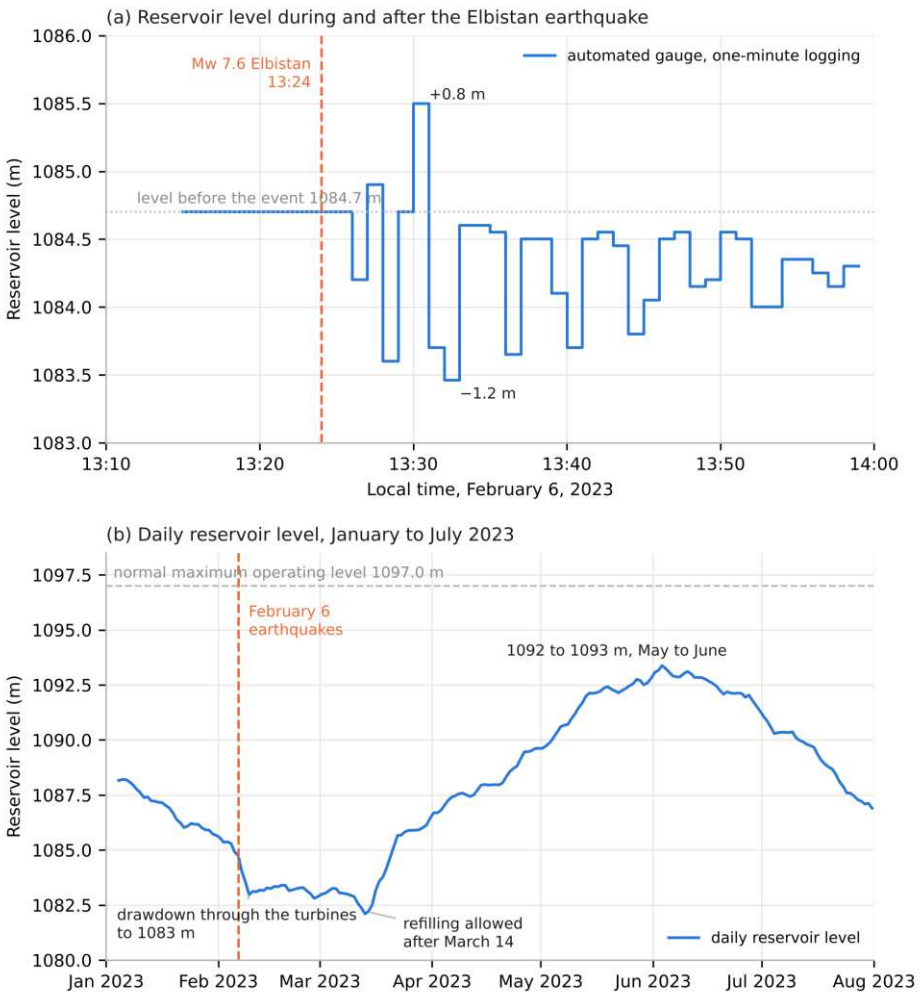
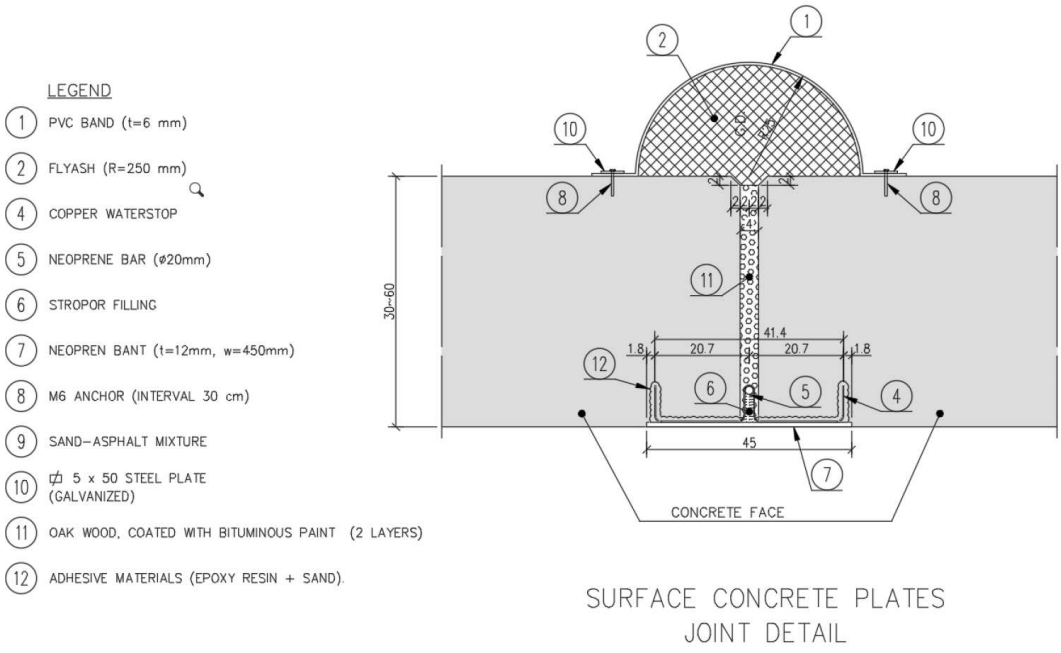


Fig. 19 Reservoir level. (a) One-minute record of the automated gauge on the upstream face during and after the Mw 7.6 Elbistan earthquake (origin time 13:24). (b) Daily level from January to July 2023, with the earthquakes, drawdown through the turbines, and refilling allowed after March 14, 2023

6.6. Waterstops and underwater inspection

The joints of the face carry a copper waterstop with a thickness of 2 mm on a neoprene band, which is encased in an external PVC band filled with fly ash and secured to the slabs by galvanized steel strips (**Fig. 20**). The PVC band and its filling are forced into an opening joint by the reservoir pressure and retained by the filter behind the slab. It serves as an upper barrier for cohesionless

586 fines of the type described in ICOLD Bulletin 141 (ICOLD 2010), which functions mainly during
587 the first years of operation, when most slab movements take place (Cooke and Sherard 1987).



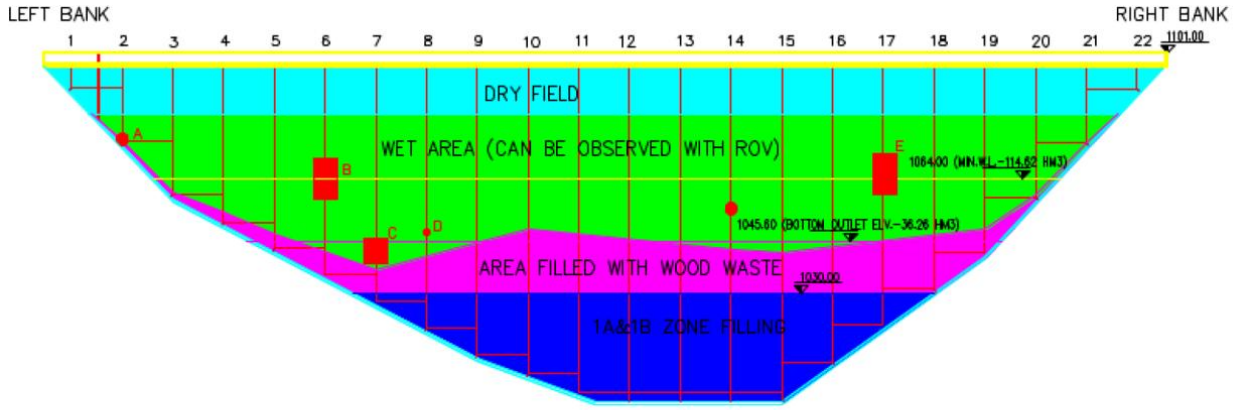
588

589 **Fig. 20** Details of the designed concrete-face joint

590

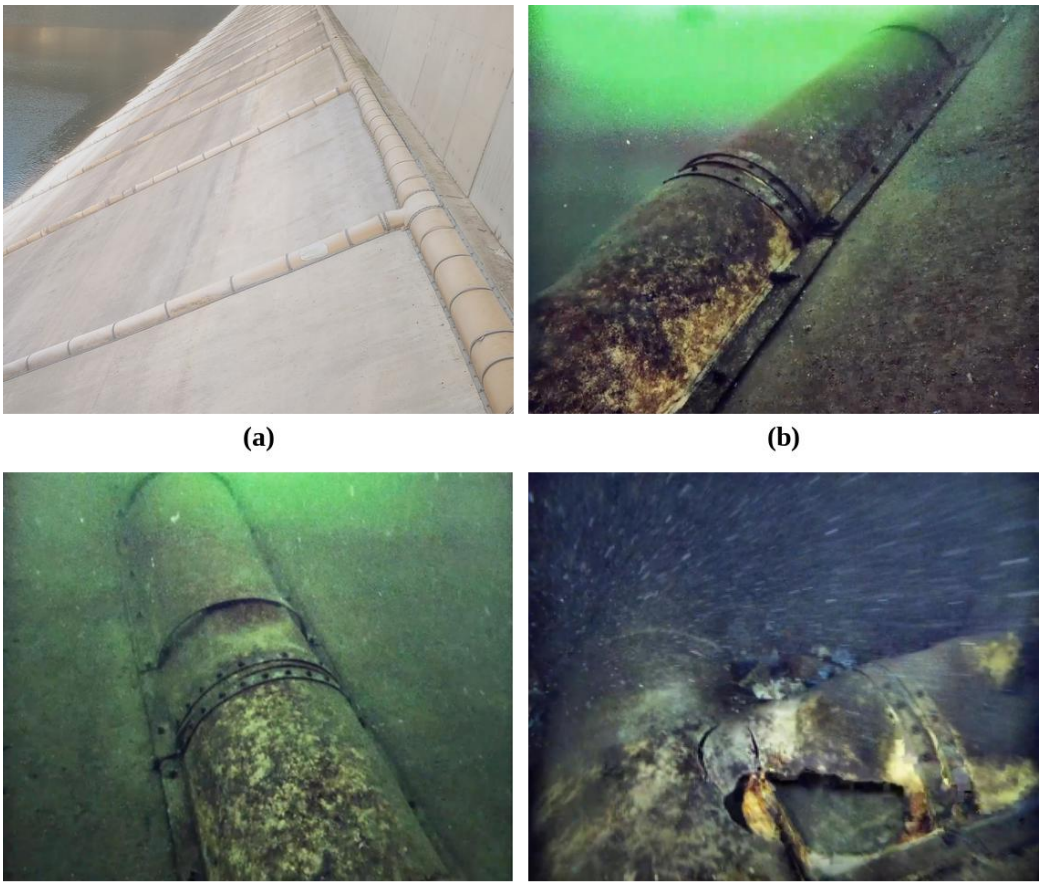
591 After the earthquakes, visual inspections identified weathering cracks in the PVC bands above the
592 maximum water level (**Fig. S8** in Online Resource 1), which is consistent with the PVC being
593 exposed to sunlight (ICOLD 2010) and unrelated to joint movement. The submerged face was
594 inspected with an ROV on March 2, 2023 (**Fig. S9** in Online Resource 1). The lower part of the
595 face was covered by the Zone 1A and 1B fill and by sediment; therefore, the inspection covered
596 approximately 47% of the face, 21% above the water surface was inspected visually, and 32% was
597 not accessible (**Fig. 21**). Under water (**Fig. 22**), the bands were full with the straps in place,
598 contracted at their fixing strips where part of the filling had moved into the joint, and, at several
599 locations between approximately 1039 and 1081 m elevation, ruptured and open with the fly ash
600 lost to the reservoir. In the five areas with the most extensive alterations (Fig. 21), the filling had

been discharged along 8–12 m of the joint length at Areas B, C, and E on joints 6, 7, and 17; the steel fixing plate was damaged at Area D on joint 8; and the band was damaged, probably by rockfall, at Area A on joint 2 near the left slope.



Area	Joint Number	Damage elevation	Explanation
A	2	1075	Damage at PVC pipe
B	6	1070-1058	Discharge of fill material
C	7	1046-1039	Discharge of fill material
D	8	1077	Damage at steel plate
E	17	1059-1071	Discharge of fill material

Fig. 21 Areas inspected using an ROV and joint numbers



606

607 **Fig. 22** Condition of the sacrificial joint covers. (a) Intact covers on the dry part of the face above
608 the water surface. (b–d) ROV frames from March 2, 2023. (b) Band full with the filling retained
609 and the fixing straps in place. (c) Band contracted at the fixing strip where part of the filling moved
610 into the joint. (d) Band ruptured and open, fly ash filling lost to the reservoir

611

612 Two distinctions govern the interpretation. The first is between the condition of the cover and the
613 function of the joint: where the filling has moved into the joint and the band is intact, the
614 observation is consistent with the function for which the upper barrier is provided, and where the
615 band has ruptured and the filling has been lost, the copper waterstop remains as the barrier, which
616 is the configuration of the central vertical joints in most CFRDs (Cooke and Sherard 1987). The
617 second is between the component and the system: whether the water barrier has remained effective
618 is a question for the hydraulic records rather than the appearance of the covers, because on a
619 nonerodible rock foundation, leakage is an economic question rather than a threat to safety, and

620 the principal surveillance of a CFRD is the measurement of leakage (Sherard and Cooke 1987;
621 Cooke 1984). The seepage record shows no sustained increase, the residual joint movements are
622 small relative to the design movements and the capacity of the copper waterstop, and the transient
623 response of TS26 is consistent with a brief local inflow sealed within days, as the upper barrier is
624 designed to do. Therefore, the joint system continued to perform its water-retaining function,
625 although the record does not prove that every inaccessible waterstop was undamaged. Because no
626 underwater inspection was made before 2023 and most of the joint movement predated the
627 earthquakes, the alterations cannot be apportioned between impounding and the seismic events,
628 and the March 2023 survey serves as a baseline for repeat inspection.

629

630 **7. Discussion**

631 In terms of the outcome, the response was consistent with the predictions. However, in terms of
632 the mechanisms, it was only partially consistent (Table 8). The abutment motion exceeded the
633 designed MCE PGA of 0.45 g by a factor of 1.6, although the dam still satisfied the performance
634 objective of no uncontrolled release with repairable damage. The slab crushing, waterstop damage,
635 and seepage increase documented at Zipingpu Dam did not develop; the crest acceleration
636 remained below the 1.90 g of the design model; the parapet settlement was a quarter of the
637 predicted 24 cm; and the foundation pore pressure response was not anticipated. However, the
638 downstream movement of the upper shell exceeded the predicted 21 cm. This analysis was limited
639 in two ways. First, most of the measurements were residuals, which were read hours after the
640 shaking; therefore, the peak dynamic predictions of the joint movement and slab stress were
641 compared with the residuals. Second, the spectral comparison rested on the two horizontal
642 components of the design record scaled to the MCE PGA. Within these limits, the input explains

most of the differences. The exceedance was confined to periods shorter than approximately 0.3 s, where the near-field Elbistan motion carried its energy, whereas the recorded spectral accelerations at the periods of the dam were 0.3 to 0.8 of the scaled design input. The causative Çardak Fault is located approximately 3 km from the dam, and its Holocene surface ruptures were documented after the design (Duman and Emre 2013; Balkaya et al. 2021b). The hazard study recognized the fault and allowed for it in the pseudo-static coefficient, and the MCE level of the dynamic verification greatly exceeded the probabilistic values. The fundamental period of the model was consistent with the measured weak-motion period within 4%, which is a consistency check and not a validation of a model whose strain-independent moduli did not represent the softening derived from the records. The crest acceleration computed for the MCE, with an amplification of 4.2, was on the safe side. It was computed for an input of 1.2 g at the model period, whereas the recorded input was 0.55 g at that period and still produced 1.658 g at the crest through its short-period energy, which was amplified by 2.3 in PGA and by 5–9 only at the fundamental period.

The permanent deformation provided a similar picture. The parapet settlement of 6 cm was a quarter of the 24 cm computed for the MCE, and the deep critical surface of the design would have moved by a few centimeters under the recorded abutment motion. The 25–39 cm measured at the crest edge and the upper berm were attributed to shear deformation of the upper downstream shell under the amplified crest motion. This pattern was shown directly by the survey vectors and was reproduced within an order of magnitude by a block driven by the crest record for a shallow mass with yield coefficients at the low end of the rockfill strength range. The 21 cm of the design was the permanent crest displacement of a continuum model under a different input, and such values are dependent on the constitutive model and analysis method as much as the input (Sharafi and Shams Maleki 2019). Consequently, the comparison is between the model displacement and the

measured one, not between two mechanisms. Therefore, the exceedance at the crest does not indicate reduced deep-seated stability; rather, it indicates the response of the crest zone, where the rockfill with the lowest confining stress accommodated the movement, which is consistent with the results reported by Mejia and Dawson (2019), who found that earthquake-induced cracking of embankment dams concentrates near the crest.

The pore pressure response of the foundation was interpreted as a coseismic pressure change in the jointed rock below the plinth with diffusive recovery based on its spatial and temporal pattern, and the interpretation does not exclude a contribution from the redistribution of foundation stresses, which the instruments could not measure. Transient pore pressure rises after strong shaking were recorded at the Aratozawa rockfill dam in 2008 (Ohmachi and Tahara 2011), and the near-field steps with exponential recovery compiled by Wang and Manga (2021) correspond to the same phenomenon in wells. The residual offsets of 1–6.5 m in the piezometers nearest the grout curtain were small relative to the 30–45 m head difference of the reservoir; however, a response of the foundation rock affects the effective stress and uplift at the plinth and is an important quantity to consider.

Considering the observations published for the same sequence, Cetin et al. (2024) estimated the PGAs to be 0.15–0.45 g for the dam sites within 50 km of the Elbistan rupture, and reported values of 0.834 and 1.464 g in the north–south direction at the abutment and crest of Kandil Dam, respectively, which are within 1% of the corrected records in this study. Under comparable estimated shaking of 0.4–0.8 g, the Kartalkaya (59 m) and Kalecik (79 m) embankment dams were displaced laterally by 60–115 cm at the crest. By contrast, Kandil Dam was categorized in the minor damage class, and its crest-to-abutment amplification of 1.2–2.3 in PGA was well below the factor of approximately 4 that Bayraktar et al. (2024a) estimated for damaged earth dams. The

reservoir stood 12.5 m below the normal maximum level, which reduced the water load; therefore, the performance is an observed outcome for that condition, and it does not verify the dam for all reservoir levels or all motions represented by the design earthquake. The favorable performance reflects the CFRD zoning, strain-dependent but stable behavior of the compacted rockfill, and joint detailing, rather than a low level of shaking.

The numerical results only transfer to high CFRDs on competent rock under near-fault shaking with comparable height, zoning, compaction, joint detailing, reservoir level, and ground motion. The transferable result is an assessment framework, which compares the recorded input with the design basis in the spectral domain, interprets the response through strain-compatible stiffness and sliding block checks, and compares the measurements with the predictions, with their types stated. The limitations are the unavailability of 37 of the 227 instrument components; the single-case nature of the record; the daily logging interval before the events, which left the maximum response of all the instruments except the accelerometers unrecorded and prevented the separation of the two main shocks; and the absence of an underwater baseline before 2023.

8. Conclusions

The 103-m-high Kandil CFRD was evaluated against the documented design predictions and the known damage mechanisms for CFRDs considering the two earthquakes that occurred on February 6, 2023, the second of which produced 0.718 g at the abutment, which was 1.6 times the MCE value of the design. The dam performed as expected for a CFRD, retaining its reservoir with minor and reparable damage and no detected sustained increase in seepage, although several mechanisms differed from the design predictions in ways that the records explain.

1. The abutment PGA exceeded the MCE value of the design by a factor of 1.6; however, the exceedance of the design accelerogram scaled to that value was confined to periods that were shorter than approximately 0.3 s. At the fundamental period of the dam, the recorded spectral acceleration was 0.3–0.5 times the design input, and the crest acceleration of 1.658 g remained below the 1.90 g of the design model.

2. The fundamental period of 0.34 s measured under weak shaking was consistent with the design model (within 4%), and its elongation to 0.44 s under strong shaking corresponded to a stiffness reduction of approximately 40% that the apparent average shear strain of 0.07% reproduced through rockfill modulus reduction curves, consistent with strain-dependent softening of the rockfill, with no large-scale instability detected and within the limits of a global deformation measure.

3. The surface survey showed downstream movement of the whole shell that decayed with depth, from 25–39 cm at the crest edge and upper berm to a few centimeters at the lower slope, with the parapet settling by 6 cm, 0.06% of the height. This is in the minor damage class reported by Pells and Fell (2002). Sliding block calculations excluded movement of the deep critical surface under the recorded motion and reproduced the order of magnitude of the upper shell movement only for a shallow mass with rockfill strength at the lower end; therefore, the pattern was interpreted as distributed shear deformation of the upper shell under the amplified crest motion, which will be confirmed by back analysis.

4. The foundation piezometers near the dam center recorded a transient increase in pore pressure of up to approximately 2 bar, which decayed with e-folding times of 10–19 h and left residuals of 1–6.5 m. Based on the pattern, this was interpreted as a coseismic response of the

733 jointed rock below the plinth with diffusive recovery. Seepage showed no sustained increase
734 relative to its historical trends, and the water remained clear.

735 5. Residual joint movements and residual slab stresses did not exceed 6 mm and 12 MPa,
736 respectively, and the transient maxima were unrecorded. The ROV survey, the first inspection of
737 the submerged joints, showed intact joints with localized loss of the sacrificial cover, which is
738 consistent with its function. Remote readings gave a safety verdict within hours, despite the
739 blocked roads.

740 This study makes three main contributions. Beyond the peak accelerations listed by Cetin et al.
741 (2024), it provides, to the knowledge of the author, the first multi-parameter record of a high CFRD
742 in the near field of a Mw 7.6 rupture, interpreted against a reconstructed design basis. It shows that
743 exceedance of a design PGA is not by itself the measure of the demand on a rockfill dam, because
744 the comparison that matters is made in the spectral domain at the periods of the dam and through
745 the strain-dependent stiffness of the fill. Moreover, the surface displacement pattern, not the
746 magnitude at one point, constrains the deformation mechanism. It identifies the transient pore
747 pressure response of the foundation rock as a phenomenon for post-earthquake assessments to
748 recognize and follow. For regulators and policymakers the results support five requirements for
749 large dams near active faults: foundation and crest accelerometers with event-triggered logging
750 that can resolve successive events, with the records transferred to the national strong-motion
751 network; post-earthquake reports that compare the recorded input with the design basis in the
752 spectral domain; a pre-event underwater baseline of the face slab joints of CFRDs and repeat
753 surveys after strong shaking; a review of the design basis of existing dams whenever
754 paleoseismological evidence of a nearby fault becomes available, as it did for the Çardak Fault in
755 2013 and 2021, and the re-evaluation that Seyrek and Tosun (2011) called for at dams near local

source zones; and piezometric follow-up of the foundation after strong shaking. These requirements address the dam safety gap that Varolgüneş (2025) identified in the literature on the earthquakes in 2023, and they complement the rapid assessment tools proposed by Bozzoni et al. (2023) for small dams.

References

Akinci A, Dindar AA, Bal IE, Ertuncay D, Smyrou E, Cheloni D (2025) Characteristics of strong ground motions and structural damage patterns from the February 6th, 2023 Kahramanmaraş earthquakes, Türkiye. Nat Hazards 121:1209–1239. https://doi.org/10.1007/s11069-024-06856-y

Ambraseys NN (1989) Temporary seismic quiescence: SE Turkey. Geophys J Int 96:311–331. https://doi.org/10.1111/j.1365-246X.1989.tb04453.x

Arias A (1970) A measure of earthquake intensity. In: Hansen RJ (ed) Seismic design for nuclear power plants. MIT Press, Cambridge, MA, pp 438–483

Avcil F, Işık E, İzol R, Büyüksaraç A, Arkan E, Arslan MH, Aksoylu C, Eyisüren O, Harirchian E (2024) Effects of the February 6, 2023, Kahramanmaraş earthquake on structures in Kahramanmaraş city. Nat Hazards 120:2953–2991. https://doi.org/10.1007/s11069-023-06314-1

Balkaya M, Ozden S, Akyüz HS (2021a) Morphometric and morphotectonic characteristics of Sürgü and Çardak faults (East Anatolian Fault Zone). J Adv Res Nat Appl Sci 7:375–392

Balkaya M, Akyüz HS, Özden S (2021b) Paleoseismology of the Sürgü and Çardak Faults, splays of the East Anatolian Fault Zone, Türkiye. Turk J Earth Sci 30:833–853. https://doi.org/10.3906/yer-2104-13

776 Bayraktar A, Ventura CE, Yang TY, Hökelekli E, Taş Y (2024a) Observed damage behavior of
777 earth dams during the 2023 Kahramanmaraş, Turkey, earthquakes. Geotech Geol Eng 42:7025–
778 7040. https://doi.org/10.1007/s10706-024-02911-4

779 Bayraktar A, Akköse M, Ventura CE, Yang TY, Hökelekli E (2024b) Onsite seismic monitoring
780 behavior of undamaged dams during the 2023 Kahramanmaraş earthquakes (M7.7 and M7.6).
781 Sensors 24:6856. https://doi.org/10.3390/s24216856

782 Bozzoni F, Misiano G, Lai CG (2023) A multi-scale tool for assessing the seismic risk of small
783 dams during emergency preparedness and response phase. Nat Hazards 118:2069–2095.
784 https://doi.org/10.1007/s11069-023-06081-z

785 Bray JD, Travasarou T (2007) Simplified procedure for estimating earthquake-induced deviatoric
786 slope displacements. J Geotech Geoenviron Eng 133:381–392.
787 https://doi.org/10.1061/(ASCE)1090-0241(2007)133:4(381)

788 Candela T, Brodsky EE, Marone C, Elsworth D (2014) Laboratory evidence for particle
789 mobilization as a mechanism for permeability enhancement via dynamic stressing. Earth Planet
790 Sci Lett 392:279–291. https://doi.org/10.1016/j.epsl.2014.02.025

791 Cetin KO, Cuceoglu F, Ayhan BU, Yildirim S, Aydin S, Demirdogen S, Er Y, Gurbuz A, Moss
792 RES (2024) Performance of hydraulic structures during 6 February 2023 Kahramanmaraş,
793 Türkiye, earthquake sequence. Earthq Spectra 40:2231–2267.
794 https://doi.org/10.1177/87552930241258295

795 Chen G, Jin D, Mao J, Gao H, Wang Z, Jing L, Li Y, Li X (2012) Seismic damage and behavior
796 analysis of earth dams during the 2008 Wenchuan earthquake, China. Soil Dyn Earthq Eng
797 41:114–123. https://doi.org/10.1016/j.soildyn.2012.05.003

798 Cooke JB (1984) Progress in rockfill dams (18th Terzaghi Lecture). J Geotech Eng 110:1381–
799 1414. https://doi.org/10.1061/(ASCE)0733-9410(1984)110:10(1381)

800 Cooke JB, Sherard JL (1987) Concrete-face rockfill dam: II. Design. J Geotech Eng 113:1113–
801 1132. https://doi.org/10.1061/(ASCE)0733-9410(1987)113:10(1113)

802 Disaster and Emergency Management Authority (AFAD) (2023) February 6, 2023 Mw 7.7
803 Pazarcık and Mw 7.6 Elbistan-Kahramanmaraş earthquakes: Earthquake Information Support
804 System (DeBiDeS). AFAD, Ankara, Türkiye

805 Duman TY, Emre Ö (2013) The East Anatolian Fault: geometry, segmentation and jog
806 characteristics. Geol Soc Lond Spec Publ 372:495–529. https://doi.org/10.1144/SP372.14

807 Durmaz S, Ülgen D (2021) Prediction of earthquake-induced permanent deformations for
808 concrete-faced rockfill dams. Nat Hazards 105:587–610. https://doi.org/10.1007/s11069-020-
809 04325-w

810 Elkhoury JE, Brodsky EE, Agnew DC (2006) Seismic waves increase permeability. Nature
811 441:1135–1138. https://doi.org/10.1038/nature04798

812 Gazetas G (1987) Seismic response of earth dams: some recent developments. Soil Dyn Earthq
813 Eng 6:2–47. https://doi.org/10.1016/0267-7261(87)90008-X

814 Guan Z (2009) Investigation of the 5.12 Wenchuan Earthquake damages to the Zipingpu Water
815 Control Project and an assessment of its safety state. Sci China Ser E Technol Sci 52:820–834.
816 https://doi.org/10.1007/s11431-009-0044-1

817 Hariri-Ardebili MA, Tosun H (2024) Dams in the wake-up call of the 2023 Türkiye earthquake
818 sequence: Insights from observed damages, risk assessment, and monitoring. Int J Disaster Risk
819 Reduct 102:104284. https://doi.org/10.1016/j.ijdrr.2024.104284

820 Hidro Dizayn (2009) Kandil Barajı ve HES kati proje raporu [Kandil Dam and HEPP final design
821 report]. Hidro Dizayn Mühendislik Müşavirlik, Ankara, Türkiye (in Turkish)

822 Hidro Dizayn (2012) Kandil Dam and HEPP, dam body concrete face joint displacement report,
823 Revision 1. Hidro Dizayn Mühendislik Müşavirlik, Ankara, Türkiye

824 International Commission on Large Dams (ICOLD) (2010) Concrete face rockfill dams: concepts
825 for design and construction. Bulletin 141. ICOLD, Paris

826 International Commission on Large Dams (ICOLD) (2016) Selecting seismic parameters for large
827 dams: guidelines. Bulletin 148. ICOLD, Paris

828 Jia JS, Xu Y, Hao JT, Zhang LM (2016) Localizing and quantifying leakage through CFRDs. J
829 Geotech Geoenviron Eng 142:06016007. https://doi.org/10.1061/(ASCE)GT.1943-5606.0001501

830 Johannesson P, Tohlang SL (2007) Lessons learned from Mohale. Int Water Power Dam Constr,
831 13 July 2007. https://www.waterpowermagazine.com/analysis/lessons-learned-from-mohale/.
832 Accessed 3 October 2026

833 Kaptan C (2007) Kandil Barajı ve HES yeri deprem risk analizi raporu [Seismic risk analysis report
834 for the Kandil Dam and HEPP site]. Report prepared for the Kandil Dam and HEPP project,
835 Ankara, Türkiye (in Turkish)

836 Konno K, Ohmachi T (1998) Ground-motion characteristics estimated from spectral ratio between
837 horizontal and vertical components of microtremor. Bull Seismol Soc Am 88:228–241.
838 https://doi.org/10.1785/BSSA0880010228

839 Leps TM (1970) Review of shearing strength of rockfill. J Soil Mech Found Div 96:1159–1170.
840 https://doi.org/10.1061/JSFEAQ.0001433

841 Luzi L, Lanzano G, Felicetta C, D'Amico MC, Russo E, Sgobba S, Pacor F, ORFEUS Working
842 Group 5 (2020) Engineering Strong Motion Database (ESM), version 2.0. Istituto Nazionale di
843 Geofisica e Vulcanologia. https://doi.org/10.13127/ESM.2

844 Makdisi FI, Seed HB (1978) Simplified procedure for estimating dam and embankment
845 earthquake-induced deformations. J Geotech Eng Div 104:849–867.
846 https://doi.org/10.1061/AJGEB6.0000668

847 Manga M, Beresnev I, Brodsky EE, Elkhoury JE, Elsworth D, Ingebritsen SE, Mays DC, Wang
848 CY (2012) Changes in permeability caused by transient stresses: field observations, experiments,
849 and mechanisms. Rev Geophys 50:RG2004. https://doi.org/10.1029/2011RG000382

850 Mejia LH, Dawson E (2019) Evaluation of earthquake-induced cracking of embankment dams.
851 Proceedings of the 2019 USSD Annual Conference, Chicago, Illinois, USA.

852 Menq FY (2003) Dynamic properties of sandy and gravelly soils. PhD dissertation, The University
853 of Texas at Austin, Austin, TX

854 Ministry of Public Works and Settlement (2007) Specification for buildings to be built in seismic
855 zones (DBYBHY 2007). Official Gazette No. 26454, 6 March 2007, Ankara, Türkiye.

856 Newmark NM (1965) Effects of earthquakes on dams and embankments. Géotechnique 15:139–
857 160. https://doi.org/10.1680/geot.1965.15.2.139

858 Ohmachi T, Tahara T (2011) Effects of the Iwate-Miyagi Nairiku earthquake in 2008, Japan on a
859 central core rockfill dam. In Dams and Reservoirs Under Changing Challenges, 79th Annual
860 Meeting of ICOLD, Lucerne, Switzerland. https://doi.org/10.1201/b11669-76

861 Ozkula G, Dowell RK, Baser T, Lin JL, Numanoglu OA, Ilhan O, Olgun CG, Huang CW, Uludag
862 TD (2023) Field reconnaissance and observations from the February 6, 2023, Turkey earthquake
863 sequence. Nat Hazards 119:663–700. https://doi.org/10.1007/s11069-023-06143-2

864 Pells S, Fell R (2002) Damage and cracking of embankment dams by earthquakes and the
865 implications for internal erosion and piping. UNICIV Report R-406, School of Civil and
866 Environmental Engineering, University of New South Wales, Sydney

867 Ramana DV, Chadha RK, Singh C, Shekar M (2007) Water level fluctuations due to earthquakes
868 in Koyna-Warna region, India. Nat Hazards 40:585–592. https://doi.org/10.1007/s11069-006-
869 9022-0

870 Rollins KM, Evans MD, Diehl NB, Daily WD (1998) Shear modulus and damping relationships
871 for gravels. J Geotech Geoenviron Eng 124:396–405. https://doi.org/10.1061/(ASCE)1090-
872 0241(1998)124:5(396)

873 Seed HB, Idriss IM (1970) Soil moduli and damping factors for dynamic response analyses. Report
874 EERC 70-10, Earthquake Engineering Research Center, University of California, Berkeley, CA

875 Seed HB, Idriss IM (1971) Simplified procedure for evaluating soil liquefaction potential. J Soil
876 Mech Found Div 97:1249–1273. https://doi.org/10.1061/JSFEAQ.0001662

877 Seed HB, Lee KL (1973) Analysis of the slides in the San Fernando Dams during the earthquake
878 of February 9, 1971. J Soil Mech Found Div 99(SM8):689–725.

879 Seyrek E, Tosun H (2011) Deterministic approach to the seismic hazard of dam sites in Kızılırmak
880 basin, Turkey. Nat Hazards 59:787–800. https://doi.org/10.1007/s11069-011-9795-7

881 Sharafi H, Shams Maleki Y (2019) Evaluation of hazardous effects of near-fault earthquakes on
882 earth dams by using EL and TNL numerical methods (case studies: Gheshlagh Oleya and Jamishan
883 dams). Nat Hazards 98:451–484. https://doi.org/10.1007/s11069-019-03702-4

884 Sherard JL, Cooke JB (1987) Concrete-face rockfill dam: I. Assessment. J Geotech Eng 113:1096–
885 1112. https://doi.org/10.1061/(ASCE)0733-9410(1987)113:10(1096)

886 Singh R, Roy D, Jain SK (2005) Analysis of earth dams affected by the 2001 Bhuj Earthquake.
887 Eng Geol 80:282–291. https://doi.org/10.1016/j.enggeo.2005.06.002

888 Skempton AW (1954) The pore-pressure coefficients A and B. Géotechnique 4:143–147.
889 https://doi.org/10.1680/geot.1954.4.4.143

890 Swaisgood JR (2014) Behavior of embankment dams during earthquake. J Dam Saf 12:35–44

891 Trifunac MD, Brady AG (1975) A study on the duration of strong earthquake ground motion. Bull
892 Seismol Soc Am 65:581–626

893 Turkish Standards Institution (TSE) (1997) TS 498: Design loads for buildings. Turkish Standards
894 Institution, Ankara, Türkiye.

895 Turkish Standards Institution (TSE) (2000) TS 500: Requirements for design and construction of
896 reinforced concrete structures. Turkish Standards Institution, Ankara, Türkiye.

United States Society on Dams (USSD) (2014) Observed performance of dams during earthquakes. Volume III. Denver, CO: USSD.

Varolgüneş S (2025) A bibliometric analysis of the 2023 Kahramanmaraş Earthquakes: trends, gaps, and policy implications. Nat Hazards 121:12461–12485. https://doi.org/10.1007/s11069-025-07305-0

Wang CY, Manga M (2021) Water and earthquakes. Lecture Notes in Earth System Sciences. Springer, Cham. https://doi.org/10.1007/978-3-030-64308-9

Yamaguchi Y, Kondo M, Kobori T (2012) Safety inspections and seismic behavior of embankment dams during the 2011 off the Pacific Coast of Tohoku earthquake. Soil Found 52:945–955. https://doi.org/10.1016/j.sandf.2012.11.013

Zhang JM, Yang Z, Gao X, Zhang J (2015) Geotechnical aspects and seismic damage of the 156-m-high Zipingpu concrete-faced rockfill dam following the Ms 8.0 Wenchuan earthquake. Soil Dyn Earthq Eng 76:145–156. https://doi.org/10.1016/j.soildyn.2015.03.014

Statements and Declarations

Funding The author received no dedicated research grant for this study. The monitoring data, surveys, and underwater inspection results were obtained within the dam safety monitoring program operated by Enerjisa Üretim A.Ş. for Kandil Dam under the supervision of the State Hydraulic Works (DSİ), and the author's time was covered by his employment with the company.

Competing Interests The author is a salaried employee of Enerjisa Üretim A.Ş., the owner and operator of Kandil Dam. The author has no other financial or non-financial interests to declare.

Author Contributions Murat Eröz is the sole author and was responsible for the study conception, compilation and analysis of the data, and writing of the manuscript.

Data Availability The monitoring records, survey data, and ROV imagery are proprietary to Enerjisa Üretim A.Ş. and relate to critical infrastructure. Therefore, they are not deposited in a public repository. Extracts may be provided by the author upon reasonable request, subject to the approval of Enerjisa Üretim A.Ş. and, where applicable, of the competent authority.

Permission to Publish Enerjisa Üretim A.Ş. reviewed the manuscript for proprietary and critical infrastructure information and authorized the use of the Kandil Dam records in this publication.

Disclaimer The analyses, interpretations, and conclusions are those of the author in his academic capacity. They do not constitute an official dam safety assessment and do not necessarily reflect the views of Enerjisa Üretim A.Ş. The official post-earthquake safety evaluations of Kandil Dam were reported to the competent authorities in accordance with applicable regulations.

931 **Tables**

932 **Table 1** Dam and reservoir characteristics

Dam and reservoir characteristics	Main zones of the dam body fill
Total reservoir volume: 438.7 hm^3 Active reservoir volume: 323.6 hm^3 Crest elevation: 1101 m Crest width: approx. 8.7 m Foundation elevation: 998 m Dam height: 103 m Max. operation water level: 1097 m Min. operation water level: 1064 m Design discharge: 107.7 m^3/s Spillway capacity: 4734 m^3/s (PMF) Dam body volume: 2,400,000 m^3 Annual average flow: 45 m^3/s Upstream slope 1:1.405 Downstream slope 1:1.4 Unsymmetrical valley Slab width: 15 m	1A (non-cohesive fine silt and sand fill) and 1B (random fill) above the plinth 2A (joint filter zone) below the plinth 2B (cushion zone) and 3A (filter zone, D_{max}: 30 cm) behind the concrete face 3B (rockfill zone, D_{max}: 60 cm) rockfill zone comprising the remainder of the dam fill 3D (D_{max}: 120 cm) downstream protective zone Concrete-face thickness varies from 0.30 m at the crest elevation to 0.60 m at the foundation level

933 D_{max}, maximum particle size of the zone material; PMF, probable maximum flood

934

935

936 **Table 2** Seismic design basis of Kandil Dam as specified in the 2007 hazard study, adopted in the
937 2009 and 2012 design analyses, and interpreted in this study

Level	PGA (g)	Specified by the hazard study (Kaptan 2007)	Adopted in the design (Hidro Dizayn 2009, 2012)	Performance objective (this paper, after ICOLD 2016)	Verification in design and key results
OBE	0.10	Probabilistic, 144-year return period, 50% probability of exceedance in 100 years	Pseudo-static coefficient 0.12 (raised from 0.11 in the hazard study for the nearby fault); input scaled to 0.10 g	At most minor damage, dam and equipment remain operational	Pseudo-static FS 1.233 at k = 0.12 (required 1.2). 3D analysis, crest acceleration 0.70 g, permanent crest displacement 0.3 cm
MDE	0.18	Probabilistic, 475-year return period, 10% probability of exceedance in 50 years	Pseudo-static coefficient 0.18; input scaled to 0.18 g	Reservoir retained, damage repairable (lower level of the SEE)	Pseudo-static FS 1.105 at k = 0.18. 3D analysis, crest acceleration 1.07 g, permanent crest displacement 3.3 cm. Estimated crest settlement 10 cm
MCE	0.45	M 7.5 on the regional sources, no PGA assigned	PGA 0.45 g, 1.5 times the 0.30 g of the second-degree zone (documents the selection, not a site-specific deterministic calculation); input scaled to 0.45 g	No uncontrolled release of the reservoir (upper level of the SEE)	Pseudo-static FS 1.067 at k = 0.20 (required 1.0). 3D analysis, peak crest acceleration 1.90 g, permanent displacement 21.2 cm downstream and 23.9 cm vertical, peak joint closure 12.3 mm and opening 15.6 mm, peak slab stress 14.5 MPa (Table 3)
Input motion		Response spectra derived from the 1986 Gölbaşı–Sürgü record	1998 Adana–Ceyhan record (Ceyhan station, Mw 6.3), scaled to the three PGA levels and high-frequency filtered, applied at the base of a massless rock foundation after the reservoir loading stage		3D finite element model, Mohr–Coulomb rockfill, pressure-dependent moduli after Seed and Idriss (1970) with K_{2max} = 150, 5% Rayleigh damping, no strength loss, no excess pore pressure. First five periods: 0.355, 0.323, 0.294, 0.270, and 0.244 s
Slope stability and freeboard		Pseudo-static coefficient 0.12 recommended	Pseudo-static limit equilibrium with k = 0.12, 0.18, 0.20; yield acceleration 0.21 g used in the settlement estimates (0.235 by extrapolation of the	Required FS 1.5 static, 1.2 OBE, 1.0 MCE	Fill crest El. 1099.0 m, parapet top El. 1101.0 m, flood level 1098.55 m, crest camber 1.0 m

Level	PGA (g)	Specified by the hazard study (Kaptan 2007)	Adopted in the design (Hidro Dizayn 2009, 2012)	Performance objective (this paper, after ICOLD 2016)	Verification in design and key results
			tabulated factors to unity)		

938

939

940 **Table 3** Dynamic analysis summary (Hidro Dizayn 2012)

		OBE (0.10 *g*)	MDE (0.18 *g*)	MCE (0.45 *g*)
Maximum crest acceleration	(*g*)	0.70	1.07	1.90
Maximum crest displacement	*x* (cm)	1.82	5.23	23.17
	y (cm)	–0.15	0.18	0.46
	z (cm)	–0.23	–2.23	–23.97
Permanent deformation after the earthquake	*x* (cm)	0.33	3.33	21.18
	y (cm)	–0.04	0.05	0.28
	z (cm)	–0.17	–2.23	–23.88
Max. closing in vertical compressible joints	(cm)	1.35	1.36	1.23
Max. opening in vertical compressible joints	(cm)	1.24	1.24	1.56
Maximum total compressive stress in the face slab	(MPa)	< 14.4	14.4	14.5

941 OBE, operating basis earthquake; MDE, maximum design earthquake; MCE, maximum credible
942 earthquake

943

944

945 **Table 4** Peak accelerations recorded at Kandil Dam

Location	Unit (*g*)	Pazarcık	Elbistan	Design MCE EQ
		Feb 6, 2023, 04:17	Feb 6, 2023, 13:24	Project phase
KND_CREST_PRIMARY[a]		0.215	1.658	1.90[c]
KND_CREST_SECONDARY[b]		0.108	0.655	N/C[d]
KND_CREST_Z		0.095	0.843	N/C[d]
KND_CREST_N		0.170	1.474	
KND_CREST_E		0.157	1.143	
KND_ROCK_PRIMARY[a]		0.064	0.718	0.450
KND_ROCK_SECONDARY[b]		0.075	0.570	0.150
KND_ROCK_Z		0.048	0.551	0.300
KND_ROCK_N		0.062	0.845	
KND_ROCK_E		0.060	0.804	

946 KND, Kandil Dam station code; MCE, maximum credible earthquake; EQ, earthquake. Peak
947 values of the baseline-corrected records. [a]Primary direction (upstream-to-downstream, 29° east of
948 north). [b]Secondary direction (along the crest, perpendicular to the primary direction). [c]Maximum
949 crest acceleration computed in the design analysis (Hidro Dizayn 2012), primary direction. [d]Not
950 computed in the design analysis, reported the crest acceleration in the primary direction

951

952

Table 5 Ground motion and response parameters in the upstream-to-downstream direction

Parameter	Pazarcık, Mw 7.7	Elbistan, Mw 7.6
Abutment rock PGA/PGV/PGD	0.064 g/10 cm/s/6 cm	0.718 g/31 cm/s/10 cm
Crest PGA/PGV	0.215 g/14 cm/s	1.658 g/70 cm/s
Arias intensity, abutment/crest (m/s)	0.18/2.6	5.0/31
Significant duration $D_{5–95}$, abutment/crest (s)	54/56	16/26
Mean period of the abutment motion (s)	0.25	0.14
Abutment S_a at 0.2/0.3/0.5/1.0 s (g)	0.09/0.07/0.06/0.04	0.98/0.90/0.39/0.25
Ratio of abutment S_a to the design accelerogram scaled to the MCE PGA, EW and NS components, at 0.1/0.2/0.3/0.44/1.0 s	0.2/0.1/0.06/0.04–0.06/0.05–0.07	3.7–4.2/1.0–1.3/0.7–0.8/0.3–0.4/0.3–0.5
Ratio of abutment S_a to the code-shaped reference at 0.1/0.3/0.5/1.0 s	0.12/0.06/0.08/0.09	2.1/0.8/0.5/0.6
Fundamental period T_1 from the Fourier amplitude ratio, primary direction (s)	0.34	0.44
Fourier amplification at T_1	16	9
Peak of the response spectral ratio (period, value)	0.31 s, 12	0.49 s, 7.7
S_a at T_1, abutment/crest (g)	0.08/0.69	0.40/2.0
Equivalent damping from the half-power bandwidth (%)	10	20–30 (upper bound)
Peak relative displacement, crest minus abutment, 0.2 to 8 Hz (cm)	3	7.3
Apparent average shear strain, peak/effective (%)	0.02–0.03/0.02	0.07/0.046

Upstream-to-downstream direction. PGA from the baseline-corrected records; spectra, intensities, and durations from the records band-pass filtered between 0.1 and 25 Hz; relative displacement and strain from the doubly integrated records band-pass filtered between 0.2 and 8 Hz. The design accelerogram is the 1998 Adana–Ceyhan record at AFAD station 0105 (Luzi et al. 2020), each horizontal component scaled to 0.45 g; the reference is the rock spectral shape of DBYBHY 2007 anchored at 0.45 g (Text S1 in Online Resource 1)

Table 6 Sliding block displacements for the Mw 7.6 Elbistan earthquake, primary direction, compared with the design prediction and the survey

Method and sliding mass	Input motion	k_y	Displacement (cm)
Newmark (1965) rigid block, deep critical surface of the design	Abutment rock record	0.15/0.21/0.235 /0.30	5 (6)/2 (3)/2 (2)/1 (1)
Newmark (1965) rigid block, full-height mass, average acceleration 0.35 times the crest record	Crest record × 0.35	0.20/0.235/0.25 /0.30	1 (4)/0 (2)/0 (2)/0 (1)
Bray and Travasarou (2007), flexible mass, T_s = 0.34 s (2.6H/V_s), $S_a(1.5T_s)$ = 0.40 g, Mw 7.6	Abutment spectrum	0.21	P($D \leq 1$ cm) 40%; median given $D > 1$ cm 2.6 (1.4 to 5.1)
Bray and Travasarou (2007), rigid form, PGA 0.718 g	Abutment record	0.21	Median 17 (9 to 33)
Newmark (1965) rigid block, upper shell, average acceleration equal to the crest record	Crest record	0.20/0.235/0.25 /0.30	61 (92)/46 (75)/40 (69)/25 (52)
Newmark (1965) rigid block, upper shell to a quarter of the height, average acceleration 0.8 times the crest record	Crest record × 0.8	0.20/0.235/0.25 /0.30	32 (55)/21 (43)/18 (39)/10 (27)
Newmark (1965) rigid block, upper shell to 0.4 of the height, average acceleration 0.65 times the crest record	Crest record × 0.65	0.20/0.235/0.25 /0.30	15 (32)/9 (23)/8 (21)/4 (13)
Design 3D analysis for the MCE, continuum permanent displacement of the crest (Hidro Dizayn 2012)	Adana–Ceyhan record scaled to 0.45 g		21.2 downstream, 23.9 vertical
Measured, survey of February 8, 2023 (Section 6.2)			Crest edge and upper berm 25 to 39 downstream; parapet 2.5 to 7.6; lower slope 5 to 7; settlement 6 at the parapet, 8 to 12 at the crest edge

k_y is the dimensionless yield coefficient, the yield acceleration being $k_y g$. Newmark values are for downstream sliding, which occurs when the ground accelerates toward the reservoir; values in parentheses are for the opposite polarity of the record. Including the vertical crest record in the yield resistance changes the values by less than 10%. The average acceleration factors 0.35, 0.65, and 0.8 follow Makdisi and Seed (1978) for masses extending to the full height, 0.4 of the height, and a quarter of the height. For Bray and Travasarou (2007) the median is conditional on $D > 1$ cm and the ranges in parentheses are the 16th to 84th percentiles. Displacements from the band-passed records (0.1 to 25 Hz), PGA of the band-passed abutment record 0.75 g, of the baseline-corrected record 0.718 g. The upper shell yield coefficient of 0.20 to 0.30 corresponds to friction angles of 46° to 52° at normal stresses of 50 to 150 kPa (Leps 1970) on the 1.4H to 1V slope

975 **Table 7** Damage classification system (Pells and Fell 2002)

Damage class		Maximum longitudinal crack width[a] (mm)	Maximum relative crest settlement[b] (percent)
Number	Description		
0	None or slight	<10	<0.03
1	Minor	10–30	0.03–0.2
2	Moderate	30–80	0.2–0.5
3	Major	80–150	0.5–1.5
4	Severe	150–500	1.5–5
5	Collapse	>500	>5

[a]Maximum likely crack width is taken as the maximum width of any longitudinal crack that occurs.

[b]Maximum relative crest settlement is expressed as a percentage of the structural height.

976

977

978 **Table 8** Measured response against the design predictions and operational references, with the
979 type of each quantity

Quantity	Design prediction or reference (type)	Measurement (type)	Like-for-like?	Measured versus predicted
Abutment rock PGA, upstream-to-downstream	MCE input 0.45 g, MDE 0.18 g (input level)	0.718 g (recorded peak)	Yes	Exceeded the MCE input by a factor of 1.6
Abutment response spectrum	Design accelerogram scaled to the MCE PGA, both horizontal components (candidate reconstructions)	Above the design input below about 0.3 s, 0.3 to 0.8 of it at 0.3 to 0.44 s (recorded)	Yes, both components of the design record	Exceeded at short periods only, below the design input at the periods of the dam
Crest PGA, upstream-to-downstream	MCE analysis 1.90 g (peak dynamic prediction)	1.658 g (recorded peak)	Yes	Below the prediction
Crest-to-abutment amplification	MCE analysis 4.2 in PGA (peak dynamic prediction)	2.3 in PGA, 9 at the fundamental period (recorded)	Yes	Below the prediction in PGA
Fundamental period	Design model 0.355 s (modal analysis)	0.34 s under weak motion, 0.44 s under strong motion (recorded)	Yes	Consistent, with strain-dependent elongation
Crest settlement	MCE analysis 23.9 cm (permanent prediction)	Parapet 6 cm, crest edge 8 to 12 cm (survey, residual)	Yes	Below the prediction, minor damage class
Downstream horizontal displacement	MCE analysis 21.2 cm at the crest (permanent prediction, continuum model)	Crest edge and upper berm 25 to 39 cm, parapet 2.5 to 7.6 cm, lower slope 5 to 7 cm (survey, residual)	Yes	Exceeded at the crest edge and upper shell, below at the parapet
Deep-seated sliding	Pseudo-static FS 1.067 at k = 0.20, yield coefficient 0.21 to 0.235 (stability analysis)	No sign of global instability (survey pattern); 2 to 3 cm computed for the deep surface under the recorded motion (inferred)	Partly	Consistent with the stability analysis
Face slab and joint damage	Slab crushing, waterstop damage, and seepage increase documented at Zipingpu under strong shaking (known mechanism, not a prediction)	No slab cracking, intact joints, localized loss of the sacrificial cover (ROV and visual inspection)	Qualitative	Did not develop
Face slab joint movement	MCE dynamic movement up to 15.6 mm (peak dynamic prediction)	Residual closure 3 mm, opening 6 mm at 17:10 (residual)	No, residual versus peak	Residuals below the peak prediction; transient maxima unknown
Face slab concrete stress	MCE analysis 14.5 MPa, characteristic strength 30 MPa (peak dynamic prediction)	Residual 12 MPa, increase 3.1 MPa at 17:10 (residual, inferred from strain)	No, residual versus peak	Residuals below the prediction and the strength; transient maxima unknown
Seepage discharge and clarity	No fixed limit, historical range at equal reservoir level (operational reference)	7 to 22 L/s at the respective reservoir levels from February 10, 2023, clear (manual readings)	Partly, no reading in the first four days	No sustained increase; 3 to 7 L/s above 2019 to 2022

Quantity	Design prediction or reference (type)	Measurement (type)	Like-for-like?	Measured versus predicted
				at the highest levels of 2023 only
Foundation pore pressure	Not considered in design (no excess pore pressure, massless foundation)	Rise of 0.5 to 1.6 bar at the first reading, 0.7 to 2.1 bar extrapolated to the event, e-folding 10 to 19 h, residual up to 6.5 m (residual and inferred peak)	No prediction	Not anticipated, interpreted as a coseismic response of the foundation rock
Wave freeboard	Fill crest El. 1099.0 m and parapet top El. 1101.0 m against the flood level 1098.55 m (design)	Reservoir at 1084.5 m with ±1.0 m oscillation (recorded)	Yes	Freeboard maintained, reservoir 12.5 m below the normal maximum level

980

981

Table 9 Response of the foundation piezometers near the dam center to the earthquake sequence

Piezometer	Elevation (m)	Depth below plinth (m)	Nearest TPC, distance (m), $\Delta\sigma$ (kPa)	Δu at 17:10 (m)	Peak at 13:24, extrapolated (m)	e-folding time (h)	Residual after six weeks (m)	Illustrative diffusivity (m^2/s)
VWP1	990	7	TPC1, 93, +74	7.9	9	16	+1.9	1×10^{-3}
VWP2	970	27	TPC1, 102, +74	14.2	15 to 16	19	+6.5	1.6×10^{-2}
VWP3	950	47	TPC1, 114, +74	16.7	18 to 22	19	0.0	5×10^{-2}
VWP8	990	7	TPC8, 72, +229	5.3	7	10	+1.3	1.6×10^{-3}
VWP4, VWP6, VWP7 (upstream of the plinth and left abutment)	990 to 1030			1.3 to 2.1		no decay	+1.6 to +2.0	
VWP9 to VWP12 (right abutment)	990 to 1050			within ±1				

Δu, excess head relative to the pre-event head versus reservoir relation; $\Delta\sigma$, step at the nearest total pressure cell at the first reading after the events (17:10 on February 6, 2023). Peaks (model-dependent extrapolations) and e-folding times from exponential plus constant fits; diffusivity from one-dimensional diffusion with the depth below the plinth as drainage length

Supplementary Files

This is a list of supplementary files associated with this preprint. Click to download.

- ESM1.pdf